Materials aspects in spin-coated films for polymer photovoltaics

Ana Sofia Anselmo

Faculty of Health, Science and Technology

Materials Science

DISSERTATION | Karlstad University Studies | 2013:3

Materials aspects in spin-coated films for polymer photovoltaics

Ana Sofia Anselmo

DISSERTATION | Karlstad University Studies | 2013:3

Materials aspects in spin-coated films for polymer photovoltaics

Ana Sofia Anselmo

DISSERTATION

Karlstad University Studies | 2013:3

ISSN 1403-8099

ISBN 978-91-7063-475-8

Distribution:
Karlstad University
Faculty of Health, Science and Technology
Department of Engineering and Physics
SE-651 88 Karlstad, Sweden
+46 54 700 10 00

Print: Universitetstryckeriet, Karlstad 2013

WWW.KAU.SE

«O binómio de Newton é tão belo como a Vénus de Milo. O que há é pouca gente para dar por isso.

óóóó — óóóóóóóó — óóóóóóóóóóóóó

(O vento lá fora).»

Álvaro de Campos

Abstract

Polymer-based photovoltaics have the potential to contribute to boosting photovoltaic energy conversion overall. Besides allowing large-area inexpensive processing, polymeric materials have the added benefit of opening new market applications for photovoltaics due to their low-weight and interesting mechanical properties. The energy conversion efficiency values of polymer photovoltaics have reached new record values over the past years. It is however crucial that stability issues are addressed together with efficiency optimization. Understanding fundamental materials aspects is key in both areas.

In the work presented in this thesis, the morphology of polymer:fullerene films and its influence on device performance was studied, as well as the effect of light exposure on the surface of fullerene films. Several polyfluorene copolymers were used for the morphology studies, where the effects of changing spin-coating solvent and of side chain engineering were investigated with dynamic secondary ion mass spectrometry (dSIMS) and near-edge X-ray absorption fine structure (NEXAFS) spectroscopy. Polymer-enriched surfaces were found in all blend films, even in the cases with homogeneous distributions in the bulk. Side chain engineering of the polymer led to gradual changes in the compositional variations perpendicular to the surface, and to small variations in the photocurrent. The electronic structure of the fullerene derivative PCBM was studied in detail and the spectroscopic fingerprint of the materials was analysed by comparison with theoretically simulated spectra. Photostability studies done in air showed that the surface of fullerene films underwent severe damages at the molecular level, which is evident from changes in the valence band and X-ray absorption spectra. These changes were explained by transitions from sp^2-type to sp^3 hybridization of the carbon atoms in the cage that resulted in the destruction of the fullerene cage.

List of Publications

The work published in this thesis was developed under the guidance of Professor Ellen Moons, Docent Krister Svensson and Professor Jan van Stam. The thesis is based on the following papers:

I. *Molecular orientation and composition at the surface of spin-coated polyfluorene:fullerene blend films* A.S. Anselmo, A. Dzwilewski, K. Svensson, E. Moons *Journal of Polymer Science Part B: Polymer Physics*, **2013**, 51 (3), pp 176-182 (DOI: 10.1002/polb.23198);

II. *Tuning the vertical phase separation in polyfluorene:fullerene blend films by polymer functionalization* A.S. Anselmo, L. Lindgren, J. Rysz, A. Bernasik, A. Budkowski, M.R. Andersson, K. Svensson, J. van Stam, E. Moons *Chem. Mater.*, **2011**, 23 (9), pp 2295-2302 (DOI: 10.1021/cm1021596);

III. *Polyfluorene copolymers with functionalized side chains: opto-electronic properties and solar cell performance* A.S. Anselmo, L. Lindgren, K. Svensson, U. Hörmann, W. Brütting, J. van Stam, M.R. Andersson, A. Opitz, E. Moons
Manuscript;

IV. *Near-edge X-ray Absorption Fine Structure study of the C_{60}-derivative PCBM* I. Brumboiu, A.S. Anselmo, B. Brena, A. Dzwilewski, K. Svensson, E. Moons
Submitted to *Chemical Physics Letters*;

V. *Light-induced modification of the electronic structure of PCBM and C_{60} films* A.S. Anselmo, A. Dzwilewski, K. Svensson, E. Moons
Manuscript.

My contribution to the papers was as follows:

Paper I: I carried out all the experimental work, including sample preparation, measurements and analysis of results, and was responsible for writing the manuscript. Corresponding author.

Paper II: I carried out the experimental work, including all the sample preparation, measurements and analysis of results, with the exception of the dSIMS measurements. I wrote the first versions of the manuscript.

Paper III: I carried out all the experimental work, including sample preparation, measurements and analysis of results, and was responsible for writing the manuscript.

Paper IV: I carried out all the experimental work. The theoretical calculations were done by I. Brumboiu and B. Brena. I. Brumboiu wrote the first version of the manuscript. Results were discussed and the manuscript was finalized in close collaboration.

Paper V: I carried out all the experimental work, including sample preparation, measurements and analysis of results, and wrote the majority of the manuscript.

Related paper not included in this thesis:

Phase behavior of liquid-crystalline polymer/fullerene organic photovoltaic blends: thermal stability and miscibility C. Müller, J. Bergqvist, K. Vandewal, K. Tvingstedt, A. S. Anselmo, R. Magnusson, E. Moons, H. Arwin, M. Campoy-Quiles, O. Inganäs *J. Mater. Chem.*, **2011**, 21, pp 10679 – 10684 (DOI: 10.1039/C1JM11239B).

Acknowledgements

First and foremost I would like to thank my supervisor Ellen Moons and my assistant supervisors Krister Svensson and Jan van Stam for all their support and encouragement, scientific and otherwise. I feel privileged for having been able to grow as a scientist and as a person with you.

A very special thank you to Jorge Morgado, who opened the door for my scandinavian adventure.

The work presented in this thesis could not have been done without the help of our collaborators. Daring as it is, particularly at this delicate close-to-final stage when brains turn into mush, I cannot help sending my heartfelt thanks to Andrzej Dzwilewski, Mats Andersson, Lars Lindgren, Stefan Hellström, Ergang Wang, Andrzej Budkowski, Jakub Rysz, Andrzej Bernasik, Mateusz Marzec, Wolfgang Brütting, Andreas Opitz, Ulrich Hörmann, Julia Wagner, Mark Gruber, Michael Kraus, Barbara Brena, Iulia Brumboiu, Christian Müller, Michael Zharnikov and Alexei Preobrajenski. You not only made the work possible, you also made every step a joy. And rest assured that if your name is missing from this list I will carry that regret forever in life.

I also want to thank my colleagues and fellow PhD students at the Department of Physics and Electrical Engineering and at the Department of Chemistry and Biomedical Sciences, past and present. You have all made my time in Karlstad very special.

To everyone that I crossed paths with in the course of these five and so years, in lab corridors and scientific workshops, in conference coffee breaks and in poster sessions, it was a sheer pleasure to be part of this bit of the world with you. Wherever I end up next, I will take it with me.

I send a warm, tight hug to all of my friends who, one way or the other, entered my life in Karlstad. I will forever be a split person thanks to you – better said,

you multiplied me. I am now many because of you, made up of irreconcilable geographies and hearts. And I am so grateful for it.

To my friends back home and spread around the world, thank you for the phone calls, the emails, the postcards and the care packages. My rushed visits were never enough for all the hugs and laughs waiting to be hugged and laughed. We need to catch up.

To my family, who never failed to make me feel home even with so many thousands of kilometers in between, I dedicate this thesis.

Finally, I thank Pedro, for the love and the warmth that somehow always managed to travel the distance and reach me. Estamos quase.

Contents

Chapter 1

Introduction

The sun is the largest source of the energy available on Earth, being primarily responsible for energy resources such as wind and wave, biomass and even oil reserves. The planet receives 162 PW of energy in the form of incoming radiation at the upper atmosphere and 86 PW of these reach the Earth's surface after reflection and absorption losses.[1] Nevertheless, the amount of solar radiation that is nowadays collected and converted directly into usable energy forms – i.e. electricity from photovoltaics or thermal energy from heat collectors – amounts to less than 0.1% of the world's present energy demands, and is several orders of magnitude lower than the sun's exergy* potential.[1,2] The largest fraction of the energy consumed globally still comes from direct combustion of fossil fuels. This dependence on fossil fuels raises environmental, economical, political, social and security issues. Along with the steady increase of energy consumption in the so-called developed world, emerging economies are also expected to contribute significantly to raising energy demand. The latest predictions point towards a 53% increase in global energy needs by 2035, rising from 17 TW in 2008 to as much as 26 TW. World net electricity generation, in particular, is expected to increase by 84% in the same period. Part of this increase will be supported by growth in electricity generation from renewable sources – the renewable share is projected to increase from the 19% mark of 2008 to 23% by 2035.[2] Photovoltaics have the potential to contribute significantly to this share.

* Exergy is a description of the theoretical extractable work from an energy source.[1]

Currently available photovoltaic (PV) technologies have the potential to cover the world energy demand single-handedly, if this demand could be completely translated into electricity needs. However PVs are not economically competitive with other electricity sources yet and storage and transportation still remain issues. Traditional PV devices are based on inorganic semiconducting materials, such as silicon (crystalline or multicrystalline). These devices have now reached efficiencies close to the theoretical maximum† and long lifetimes‡, but are still expensive to manufacture. They require high quality silicon which implies high temperature and high pressure engineering and leads to an energy payback time of around 2 to 4 years, in the case of crystalline silicon systems.[3] This is expected to improve as efficiency of devices and fabrication methods are optimized, particularly the purification and crystallization processes. Decreasing the costs for manufacturing and for materials is then an important challenge for traditional PVs. Other inorganic PV technologies include thin film photovoltaics, such as $CuInGaSe_2$ and CdTe solar cells, where significantly less material is used.

Organic photovoltaics (OPVs) are an exciting alternative to inorganic solar cells. Photovoltaic devices based on semiconducting polymers, in particular, can be processed from solution at low temperatures allowing the use of high throughput inexpensive printing techniques. Moreover, these polymers generally have high absorption coefficients and hence it is possible to produce very thin solar cells, using less material and lowering production costs further. Module manufacture impacts greatly on the final electricity cost and developing (inexpensive) OPVs could contribute to boosting photovoltaic energy generation overall. Besides allowing large-area inexpensive processing,

† Record efficiencies are 25% for crystalline and 20.4% for multicrystalline silicon-based modules[4], while commercially available products normally have an efficiency of 10 – 15%. The theoretical efficiency limit (Shockley-Queisser limit) for single p/n junction solar cells is 30%.[191]

‡ Commercially available products are warranted a lifetime of generally 25 years, with a limited loss of power output (about 10 to 20% decrease).

polymeric materials have the added benefit of opening new market applications for photovoltaics due to their low-weight and interesting mechanical properties. Polymer-based solar cells can be integrated in other materials, e.g. building components, significantly lowering installation costs. Incorporation in textiles, paper and plastics also opens the field for end-user, mobile applications. Additionally, both the electro-optical and the mechanical characteristics of the semiconducting polymers can be chemically tuned, which is an excellent tool for product development.

The success of polymer photovoltaics as a viable technology is predicated on the development of three main areas: processing, efficiency and stability. Over the last 20 years, great progress has been made in terms of efficiency and, to a smaller extent, processing. Stability, however, has remained relatively unexplored. Efficiency issues, in particular, have been an important focus of the research community and the knowledge accumulated so far has led to a steady improvement of OPV performance.[4] Recently, an encouraging efficiency value of over 10% was certified for polymer-based solar cells.[4,5] As viable commercialization of OPV seems increasingly more likely, resolving stability issues becomes imperative. Performance improvements have most certainly been due not only to the development of new materials and device architectures but also to a better understanding of the underlying mechanisms of the photovoltaic process in polymer solar cells. Likewise, increasing device lifetime will require a deeper knowledge of degradation pathways and failure modes, and how these are related to diminished photovoltaic performance, along with the design of more stable materials and better encapsulation techniques. In both areas, understanding the fundamental mechanisms is key to the further development of OPV technology.

The most successful type of polymer solar cell to date is based on thin films of a blend of two materials: a light-absorbing conjugated polymer (the electron donor) and a solution-processable fullerene derivative (the electron acceptor).

These two components are intimately mixed forming a bulk heterojunction (BHJ) structure, in which the interfacial area between the two materials is large. The advantage of this particular type of structure over, for instance, bilayer structures[§] is related to the fact that, in organic photovoltaic cells, the absorption of light does not generate a mobile charge immediately. Instead, an excited state, an electron/hole pair called an exciton, is created. For the solar cell to generate current, this exciton needs to be separated into mobile charges, i.e. an electron and a hole. This separation can occur at the boundary of two materials with different electron affinities, where the electron is transferred from the donor to the acceptor material. Only when the exciton is dissociated and mobile charges are generated can these be transported to the electrodes and collected. A large interfacial area, like in the case of a BHJ structure, maximizes the number of sites available for dissociation within reach of the exciton before it decays. This means that the two materials should be sufficiently well mixed that donor and acceptor domains are not larger than twice the exciton diffusion length. On the other hand, transport of the mobile charges occurs preferentially through the donor material for the hole, and through the acceptor material for the electron. This poses an interesting challenge in the preparation of the blend film. While the interfacial area must be maximized it is also crucial to guarantee uninterrupted pathways for each of the free charges to reach the appropriate electrodes. The morphology of the active layer, i.e. the distribution of electron donor and electron acceptor materials in the film, is thus of great importance for the performance of polymer solar cells.

The optimum morphology is generally not thermodynamically stable and may change with time leading to lower power conversion efficiencies. Photovoltaic performance and lifetime is also affected by chemical modification of the active layer components (donor and acceptor materials). Further issues occur in the remaining structural layers and interfaces of OPVs, but it is the active layer

[§] In bilayer structures the donor and the acceptor materials are deposited as two separate layers on top of each other.

which is most prone to degradation. A deeper understanding of the fundamental relation between film preparation, final film morphology and device performance is essential in order to understand the influence of the active layer structure on each step of photovoltaic performance and establish fabrication strategies that lead to more efficient solar cells. At the same time, device lifetime must increase in order for polymer photovoltaics to be able to enter the photovoltaic market. Elucidating and controlling the mechanisms of degradation is crucial for the development of technological solutions that lead to lifetimes acceptable for commercial use.

In the work presented in this thesis, the morphology of polymer:fullerene films and its influence on device performance was studied, as well as the effect of light exposure on the surface of fullerene films. Several polyfluorene copolymers were used for the morphology studies, where the effects of changing spin-coating solvent and of side chain engineering were investigated with dynamic secondary ion mass spectrometry (dSIMS) and near-edge X-ray absorption fine structure (NEXAFS) spectroscopy. Polymer-enriched surfaces were found in all blend films, even in the cases with homogeneous distributions in the bulk. Side chain engineering of the polymer led to gradual changes in the compositional variations perpendicular to the surface, and to small variations in the photocurrent. The electronic structure of the fullerene derivative PCBM was studied in detail and the spectroscopic fingerprint of the materials was analysed by comparison with theoretically simulated spectra. Photostability studies done in air showed that the surface of fullerene films underwent severe damages at the molecular level, which is evident from changes in the valence band and X-ray absorption spectra. These changes were explained by transitions from sp^2-type to sp^3 hybridization of the carbon atoms in the cage, resulting in the destruction of the fullerene cage.

The work was done in collaboration with the Polymer Electronics group, at Chalmers University of Technology (Sweden); the Macromolecular Nanofilms

for Electronics and Biotechnology group, at Jagiellonian University and AGH University of Science and Technology (Poland); the Organic Semiconductors group, at University of Augsburg (Germany); and the Materials Theory group, at Uppsala University (Sweden). All NEXAFS studies were done at the national facility for synchrotron-based research MAX-lab in Lund, Sweden.

Chapter 2

Polymer photovoltaics

The beginning of organic photovoltaics dates back to 1959, when anthracene was first used to make a solar cell by Kallman and Pope.[6] In the 1970's, it was found that even some polymers displayed semiconducting behaviour and could be doped in order to achieve conductivities similar to those of inorganic semiconductors or metals.[7] This discovery was recognized with the Nobel Prize in Chemistry in 2000, awarded to Heeger, MacDiarmid and Shirakawa.[8] However, the efficiency of single material organic solar cells was disappointingly low.[9] The field gained pace after 1986 when Tang and co-workers introduced a second layer.[10] In their devices, they used two molecules, one an electron donor and the other an electron acceptor. This donor/acceptor concept was successfully applied to a combination of a polymer and a new acceptor material (buckminsterfullerene) in 1992, independently by Sariciftci et al.[11] and Morita et al.[12] In that same year, Hiramoto et al. developed the donor/acceptor concept by co-evaporating two small molecules in high-vacuum conditions, leading to an intimate mix of the components.[13] Three years later, this new device structure (the blend heterojunction, BHJ) was fully applied to working organic photovoltaics by Yu et al. [14] in polymer:fullerene blends and by Halls et al. in polymer:polymer blends,[15] independently. Polymer photovoltaics have, since then, focused a lot of efforts on the development and optimization of the BHJ structure.

2.1 Polymer semiconductors

Organic semiconductors are materials with a conjugated π-system, and they can be either of molecular (so-called small molecules) or of polymeric nature. This spatially extended π-system plays a crucial role in defining their electrical and optical properties, which can to some extent be tailored chemically.[16] In this section, attention shall be given to conjugated polymer systems, although many of the arguments apply to organic semiconductors in general.

The simplest conjugated polymer is polyacetylene (see figure 2.1) and is taken as an example here. Of the four valence electrons of carbon ($2s^2 2p^2$), three sp^2 hybrid orbitals form three σ-bonds, one with each of its two neighbouring carbons (forming the backbone of the polymer) and one with a hydrogen atom. The remaining fourth electron is located in a p orbital, perpendicular to the backbone plane. A schematic diagram of these bonds is shown in figure 2.2.

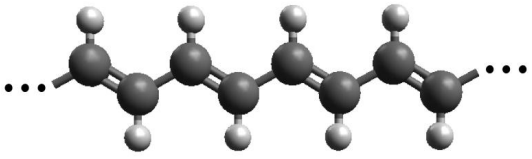

Figure 2.1 Ball-and-stick model of *trans*-Polyacetylene.

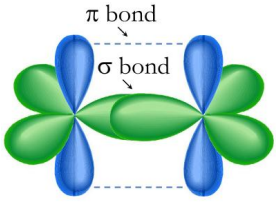

Figure 2.2 Schematic diagram of the bonding system in conjugated polymers: the sp^2 orbitals of neighbouring carbon atoms overlap to build a σ bond and the p orbitals overlap laterally to form a π bond.

The overlap of the p orbitals of adjacent carbons in the backbone forms the π-system, which is delocalized over the polymer backbone. The conjugation length is defined by the effective overlap of the p-orbitals, which is maximized when the polymer adopts a planar configuration. While the σ bonds maintain the physical structure of the polymer, the electrons in the delocalized π-system, which are more loosely bound, dominate the optical and electronic characteristics of the material.[17,18] Because there are many electrons contributing to this system in a polymer chain, these molecular orbitals become broad quasi-continuous energy bands that are comparable to the conduction and valence bands of inorganic semiconductors. In this sense, the highest occupied molecular orbital (HOMO) corresponds to the energy level at the top of the valence band, and the lowest unoccupied molecular orbital (LUMO) is analogous to the first available energy level in the conduction band, as illustrated in figure 2.3.

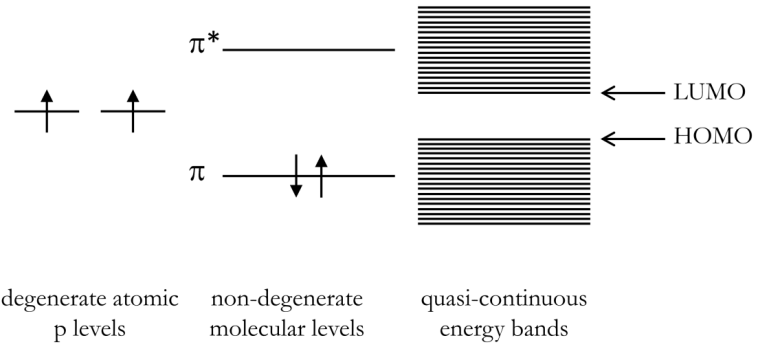

Figure 2.3 Schematic diagram of the formation of molecular orbitals and of valence and conduction bands: p atomic orbitals combine to form non-degenerate energy levels when two atoms are brought together. Quasi-continuous energy bands are formed when a large number of atoms contribute to the delocalized system. (Adapted from reference 17)

Admitting a one-dimensional extended system and equal bond lengths, it would follow that the π-electron band formed by delocalization of the π-electrons along the polymer chain would be half-filled and the polymer would have metallic behaviour. However, in real polyacetylene the bond lengths are not equal. There is an alternation of longer (single) and shorter (double) bonds, as a consequence of Peierls distortion, which leads to the formation of two π-type molecular orbitals: π (bonding) and π* (anti-bonding). They are separated by an energy gap, E_g, and only the lowest energy level is occupied. Therefore, the polymer adopts semiconductor behaviour, and not metallic.[19,20]

The higher the number of overlapping p orbitals (and so the higher the number of electrons participating in the π-system), the wider the bands and the smaller the energy gap between them – i.e. narrower bandgaps for longer effective conjugation lengths. Any changes in the polymer structure that influence conjugation, such as deviations from a planar structure, twists of the backbone or addition of side groups that prevent overlap of chains, will influence the energy gap as well. It is also possible to manipulate the characteristics of the bandgap through doping[**] processes. Consequently, there is an opportunity to tailor the bandgap, and with it the electronic properties of polymeric molecules, through chemical synthesis or doping.

Semiconducting polymers generally have a bandgap that ranges from 1.5 to 3 eV (850 – 400 nm). This is within the energy range of visible light photons which makes these polymers suitable materials for optoelectronic devices. Photons whose energy is larger than the bandgap can excite an electron from the HOMO to the LUMO of the polymer. The result of this photoabsorption is the creation of an excited state where an electron and a hole are bound together by Coulomb forces, forming an electron-hole pair (also

[**] Doping consists of the introduction of extra donor (n-type doping) or acceptor (p-type doping) energy levels within the bandgap by adding a foreign element, which increases conductivity.

called an exciton). Exciton binding energies in polymers are of the order of a few hundred meV, much higher than the thermal energy at room temperature (kT ~ 26 meV). Therefore no thermal dissociation of excitons will occur and a strong enough electric field is necessary in order to separate the exciton into free charges.[21,22] Exciton dissociation is generally achieved at the interface of the electron donor polymer with an electron acceptor material, such as a fullerene derivative. The different processes involved in photovoltaic energy conversion in polymer solar cells will be addressed further in section 2.3.

Polymer semiconductors are not crystalline materials and have low charge carrier mobilities ($\mu < 1$ cm^2/Vs), two to four orders of magnitude lower than typical mobilities in inorganic semiconductors.[22] However, their high absorption coefficients ($\alpha > 10^5$ cm^{-1})[9] make it possible to use only very thin layers. A thickness of approximately 100 nm is sufficient to absorb most of the incident light within the absorption range of the material. Besides the obvious advantage of using less material, thin layers mean that the free charges have a much shorter distance to travel before reaching the electrodes than in the case of inorganic devices. Low carrier mobility in the polymer is then not necessarily the performance limiting step in polymer photovoltaics.[9] Efficiency may be further limited by poor spectral overlap with the solar spectrum, inadequate energy level offset with the acceptor material or poor morphology.

Several polymer synthesis strategies have been successful in addressing these issues and improving solar cell performance. Extending the conjugated system by selecting monomers with rings that induce planarization of the polymer backbone will shift the absorption range towards longer wavelengths. Additionally, it favours π-stacking of the polymer chains, which can contribute to lower bandgaps and modify the morphology. Alternating electron-rich with electron-poor units, in a push-pull structure, also reduces the optical bandgap of the polymer and is a commonly used strategy. Changing the heteroatoms in

the rings may have a significant effect on the LUMO level and can be used to optimize the energy level offset with the acceptor material. The nature and amount of side chains can be used to tune the miscibility with the acceptor and affect morphology. Further information can be found in recent reviews.[23–26]

2.2 Fullerenes

Fullerenes are an interesting family of carbon allotropes in which carbon atoms are arranged into 12 regular pentagons and an arbitrary number of hexagons, forming spherical or spheroid hollow clusters.†† Some examples of fullerenes can be found in figure 2.4. The cages are formed by sp^2-type hybridized carbon atoms, each bonded to three others by three single (σ) bonds and one double (π) bond. To allow the formation of pentagons, and the subsequent geometrically closed molecular structure of fullerenes, the sp^2-bonding occurs on a curvature.[27] This means that each sp^2-carbon and its three neighbouring atoms cannot be coplanar, as in the case of e.g. graphite or polyacetylene

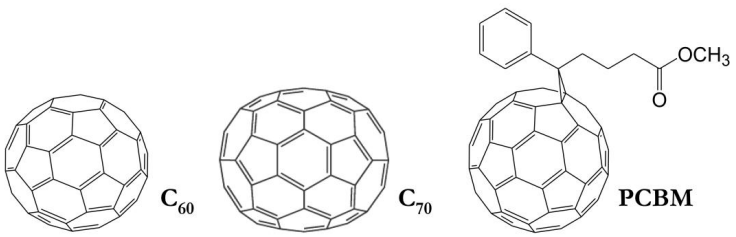

Figure 2.4 Molecular structure of C_{60}, C_{70} and [60]-PCBM.

(illustrated in figures 2.1 and 2.2), and instead bonds to form an angle larger than 90° between the p-orbital axis and each C-C bond vector (figure 2.5).[28] This curvature introduces strain in the molecule, making it unstable. Stable structures can be achieved for fullerenes that avoid edge-sharing pentagons (i.e.

†† The smallest possible fullerene is C_{20}, built with 20 carbon atoms arranged into 12 pentagons and zero hexagons.

when each pentagon is surrounded by 5 hexagons), in this way preventing high local curvature. The smallest fullerenes that fulfil this isolated pentagon rule are C_{60} and C_{70} (see figure 2.4).[27]

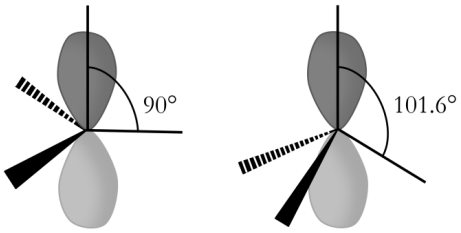

Figure 2.5 Angle between the p orbital axis and the C-C bond vectors in graphite (left) and in C_{60} (right).[28]

C_{60} (buckminsterfullerene) was first discovered in 1985,[29] for which the 1996 Nobel prize in Chemistry was awarded,[30] but it was the development of a simple way to produce macroscopic amounts of the material[31] that provided the necessary means to further develop this field of research. Due to its highly symmetrical configurations and unique physical and chemical properties, C_{60} and related compounds are of interest in areas as diverse as astrophysics, materials science, or biomedicine.

The electrical properties of C_{60}, and of other native fullerenes such as C_{70}, are particularly suitable for use in photovoltaic devices. These include good electron mobilities,[32,33] isotropy of electronic properties due to high 3D symmetry,[34] adequate energy level positions for combination with most conjugated polymers,[35] subpicosecond photoinduced electron transfer when combined with several conjugated polymers,[11,36] and slow charge recombination.[34,37] Moreover, good crystal packing and fast precipitation kinetics associated with a propensity to form clusters can be advantageous for uniform film formation and appropriate phase separation in blend films.[34] However, issues such as insolubility in common solvents,[38] low-lying LUMO

level[#] and low optical absorption in the solar spectral range have spurred the development of new fullerene derivatives that could improve these properties while preserving the positive characteristics of the native fullerene molecules. This has generally been achieved by attaching multiple solubilising groups to the fullerene cage, as was the case with [60]-PCBM (henceforth referred to as PCBM). Its chemical structure can be found in figure 2.4. While maintaining the electrical properties of C_{60}, PCBM is soluble in common solvents allowing the use of simplified film processing techniques. This combination of characteristics has turned it into the most popular electron acceptor used in organic photovoltaics since it was first synthesized.[39] Additionally, the saturation of the double bonds in the carbon cage, which is a direct consequence of addend attachment, has the effect of pushing the LUMO closer to vacuum, which addresses the issue of the low-lying LUMO level mentioned above.[35,40] Improving absorption in the visible range is achieved by using derivatives based on higher order fullerenes,[34,35,37,40] which has been successfully done for instance with [70]-PCBM.[41]

Although material design for polymer photovoltaics has been mainly focused on novel high-performance polymers, developing new fullerene derivatives is also underway and has the potential to lead to significant advances in organic photovoltaics.[35,40]

2.3 Physics of polymer solar cells

Organic solar devices are commonly layered structures comprised of a photoactive layer sandwiched between two electrodes. At least one of the electrodes, usually the bottom one, is transparent in order to allow light to reach the light-absorbing polymer. Usually a layer of indium tin oxide (ITO) on

[#] A low lying LUMO level can limit photovoltaic performance in devices where the fullerene is combined with an electron donor organic compound. This subject is further developed in sections 2.3 and 4.6.

a glass substrate covered with PEDOT:PSS (poly(3,4-ethylenedioxy-thiophene):poly(styrene-sulfonate)) is used. While ITO is the anode, PEDOT:PSS acts mainly as a surface-smoothener and increases the work function enhancing hole extraction. ITO has a rather rough surface which, in a sandwich-type structure, could lead to direct contact between the electrodes. The top electrode (the cathode) is normally an evaporated layer of a low work function metal. Aluminium is often used, generally evaporated on top of a thin film of lithium fluoride (LiF), which serves to improve device performance and protect the polymer film during cathode deposition.[42] Figure 2.6 gives a schematic account of the general structure of a polymer solar cell.

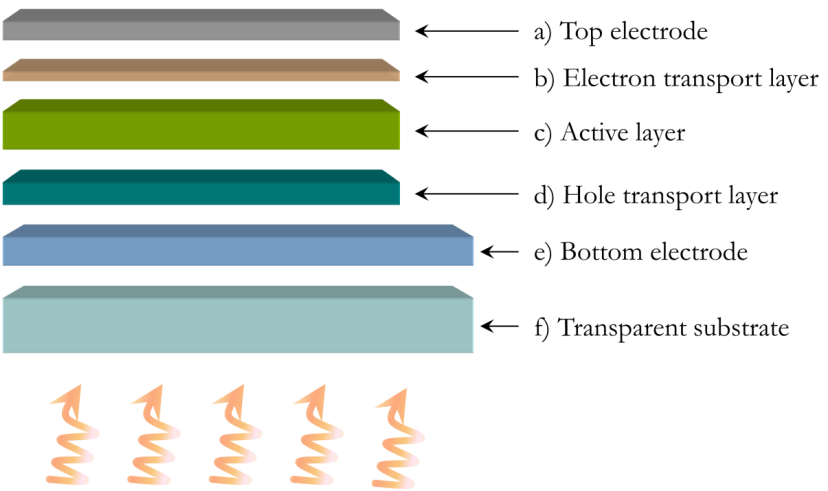

Figure 2.6 General structure of a polymer solar device. Typical thickness of each layer: a) 60 – 300 nm; b) 1 – 2 nm; c) 100 – 200 nm; d) 80 – 100 nm; e) ~ 100 nm, and f) 100 – 1000 μm. (note: these values are merely indicative and vary depending on the materials used)

In a solar cell, photon absorption creates an exciton in the polymer by promotion of an electron from the HOMO to the LUMO. As mentioned previously, the electron and the hole can only be separated if a sufficiently strong electric field is present. The exciton binding energy in organic devices is

at least a few hundred meV and generally the electric field resulting from the different work functions of the electrodes is not enough to efficiently generate free charges. As a consequence, homojunction devices, where the photoactive layer is composed of a single material, are not efficient in organic photovoltaics and the use of donor-acceptor (D/A) interfaces in heterojunction configurations is necessary. In these configurations, two different materials with different valence and conduction bands, or the equivalent HOMO and LUMO levels, are combined. It is then the offset between the energy levels of the donor and of the acceptor (primarily the energy difference between their LUMO levels) that drives the dissociation of the exciton into separate charges. This offset needs to be at least as large as the exciton binding energy, i.e. a few hundred meV, in order for the charge separation process to be efficient. This in turn reduces the maximum voltage output that can be obtained from organic solar cells, which is generally defined by the energy difference between the HOMO of the electron donor and the LUMO of the electron acceptor.

The five main processes that govern heterojunction solar cell performance are: (a) photon absorption and exciton formation; (b) exciton diffusion; (c) electron transfer and exciton dissociation; (d) charge transport through the two electron- and hole-transporting phases toward their respective electrodes; and (e) charge collection at the interfaces with the two electrodes. Figure 2.7 is a schematic diagram of the processes involved in organic photovoltaics, drawn for an ideal bilayer with sharp interfaces, in short-circuit conditions.

(a) photon absorption and exciton formation

The first requirement for efficient photon absorption is a high transparency of the electrode through which the light must pass in order to reach the photoactive material. Reflection losses must be minimized. The next basic requirement is that the absorption spectrum of the active material matches solar irradiation as well as possible. On the surface of the earth, the largest photon

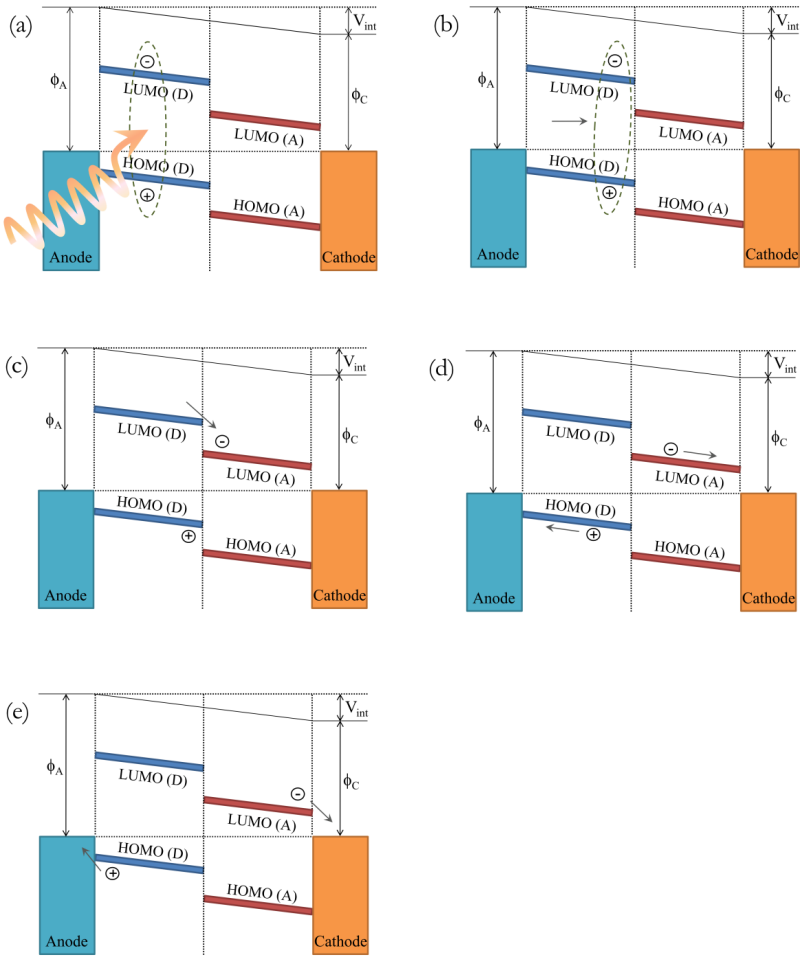

Figure 2.7 Simplified energy diagrams of the main steps of photovoltaic energy conversion in an organic solar cell, in short-circuit conditions: (a) photon absorption and exciton formation; (b) exciton diffusion to a D/A interface; (c) electron transfer and exciton dissociation; (d) charge transport; and (e) charge collection at the electrodes. ϕ_A and ϕ_C are the work functions of the anode and of the cathode, respectively, and V_{int} is the internal electric field, which in this situation is a result of Fermi level alignment of the electrodes.

flux is in the range of 600 to 1000 nm (2.0 – 1.3 eV),[43] so materials for terrestrial applications should have an optical excitation energy gap below these values for optimized photon absorption. These conditions fulfilled, the promotion of an electron from the HOMO to the LUMO of the organic material generates an electron-hole pair bound by Coulomb attraction forces – the exciton.

(b) exciton diffusion

Once generated, the exciton migrates three-dimensionally through the material – by intra and interchain energy transfer, in a diffusion-restricted mechanism. The exciton has a short lifetime, with diffusion lengths in the range of 1 to 10 nm.[9] Decay channels include radiative decay with luminescent emission, vibronic and thermal decays, and dissociation at specific sites. A D/A interface needs to be in the range of the exciton diffusion length in order for dissociation to compete with the other decay processes.

(c) electron transfer and exciton dissociation

Exciton dissociation separates the exciton into two mobile opposite charges. Dissociation of excitons at D/A interfaces can contribute to the photocurrent, provided the charges do not recombine before being collected at the electrodes.

The charge transfer occurs when both the electron affinity (EA) and the ionization potential (IP) of the electron acceptor are larger than the ones of the electron donor, and the energy difference between the two LUMOs (δE) is greater than the exciton binding energy. This corresponds to process 3 in the energy diagram of figure 2.8.

If light is absorbed by the acceptor material, excitons can also be created there – and process 7 in figure 2.8 refers to an electron back transfer (transfer of a hole from the acceptor HOMO to the donor HOMO). Processes 1 and 5 refer

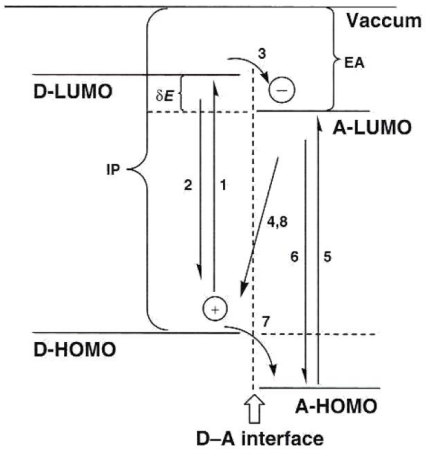

Figure 2.8 Schematic energy band diagram and processes of a donor/acceptor interface.[44]

to excitation, whereas 2 and 6 refer to the corresponding emission. Processes 4 and 8 indicate possible interfacial recombination phenomena that lead to loss of charge carriers. Recombination can be *geminate*, when a recently separated electron – hole pair recombines due to a too weak field, or *non-geminate*, when an electron and a hole generated from dissociation of different excitons recombine.[9,44]

(d) charge transport

In polymer photovoltaic devices, which generally lack long-range order when processed from solution, carrier transport to the electrodes occurs mainly by a hopping process – charges hop from one localized state to another.[9] There are also contributions from drift processes that are induced by a built-in electric field across the photoactive layer created by the difference in the work function of the electrodes.[45]

(e) charge collection at the electrodes

The transfer of an electron or a hole to the respective electrode is dependent on the geometry, the topology and the formation of the interface. A significant efficiency loss may occur at the electrodes. In an ideal configuration the LUMO and HOMO energy levels of the acceptor and donor materials match the Fermi levels of the correspondent cathode and anode, creating an ohmic contact, and the charges can be efficiently extracted to the external circuit.

The performance of photovoltaic devices is commonly assessed by analysing its current-voltage dependence in the dark and under standard illumination. A description of these curves and the relevant solar cell parameters is given in section 4.6.

2.4 Morphology of the photoactive layer

The development of heterojunction photoactive layers, which are based on donor-acceptor interfaces, was an important breakthrough in organic photovoltaics. Two main architectures are: the *bilayer heterojunction*, in which the two materials, donor and acceptor, are deposited as two separate layers on top of each other; and the *bulk* or *dispersed heterojunction* (BHJ), in which donor and acceptor species are blended together in solution or deposited simultaneously. A schematic representation of these heterojunctions is shown in figure 2.9.

As discussed in the previous section, efficient transport of charge is of major importance in organic solar cells. In bilayer heterojunctions, the free charges have uninterrupted pathways to the respective electrodes from the place where they are created. However, the D/A interface area within the range of the excitons' diffusion length is smaller than in the case of a BHJ and therefore fewer free charges can be created. On the other hand, for BHJs there is a

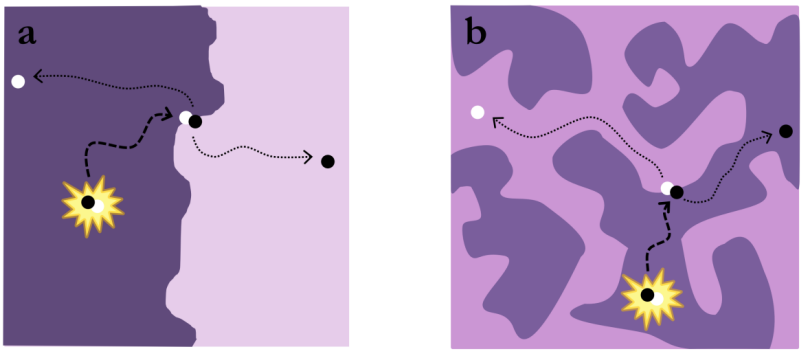

Figure 2.9 Main architectures for the photoactive layer in polymer solar devices: (a) bilayer heterojunction and (b) bulk heterojunction. The exciton, created in the light-absorbing material, is dissociated at a D/A interface and the free charges travel toward the respective electrodes.

concern that a continuous network of percolation pathways that allows efficient transport and collection of charges at the electrodes may not be formed. In fact, while the interfacial contact area between acceptor and donor materials in a blend increases the number of free charges, it is also likely that isolated islands and bottlenecks are formed that effectively act as charge traps. Moreover, in BHJs the electrode/photoactive layer interface is complex to describe, since each electrode will be in contact with both the hole-transporting (donor) and the electron-transporting (acceptor) material. A compromise between these two architectures is a diffuse bilayer, in which the two separate layers of acceptor and donor materials are made to interdiffuse at the boundary between the two materials, effectively increasing interfacial area while still maintaining uninterrupted pathways to the electrodes.

To date, the bulk heterojunction architecture is still the main device structure for high-performance organic photovoltaics, not the least because of its simple one-step fabrication process. The challenge remains to tailor the BHJ morphology toward optimized device fabrication and performance. Ideally, this implies self-generated phase separation (at room temperature and atmospheric

pressure) between the two components of the blend on a scale of 20 – 30 nm, a so-called bicontinuous interpenetrating network, which ensures efficient exciton dissociation and delivery of the charges to their respective electrodes.[46]

Controlling and understanding the morphology in BHJ is crucial to the further development of more efficient polymer photovoltaic devices. New experimental techniques are needed, able to probe the composition of blend films on the nanometer scale; these will be an invaluable tool for the correlation of blend film nanostructure with device performance.

The morphology of the blend films depends on the conditions of film formation. The drying process will determine the morphology of the resulting films – phase separation mechanisms can be halted at different non-equilibrium situations. When prepared from solution, besides specific conditions relating to the type of deposition technique used, final film morphology is dependent on molecular weights,[47] solvents,[48–53] blend ratio, relative solubilities,[54] etc.

2.4.1 Thermodynamics of phase separation in polymer blends

It is a common procedure to blend a polymer with another polymer or particle in order to achieve a resulting material with different, more attractive characteristics (mechanical, chemical or physical) than the original species. Obtaining a homogeneous mixture calls for specific concentration and temperature values since polymers are generally immiscible. Deviations from the concentration and temperature values that allow miscibility will drive the system to separate into different phases. The degree of separation is dependent on the rate of the concentration/temperature change – if the change is slow enough the separation tends to be complete, while if it is fast it freezes the mixture into an intermediate state.

Thermodynamically, a system is spontaneously miscible when its free energy of mixing, ΔG_{mix}, is negative. ΔG_{mix} is given by:

$$\Delta G_{mix} = \Delta H_{mix} - T\Delta S_{mix} \tag{2.1}$$

ΔH_{mix} is the enthalpy of mixing, ΔS_{mix} is the entropy of mixing and T is the temperature. For polymer solutions, the entropy and enthalpy terms are calculated according to the Flory-Huggins theory. The solution is viewed as a lattice where each site is either occupied by a solvent molecule or a polymer repeating unit, as depicted in figure 2.10.

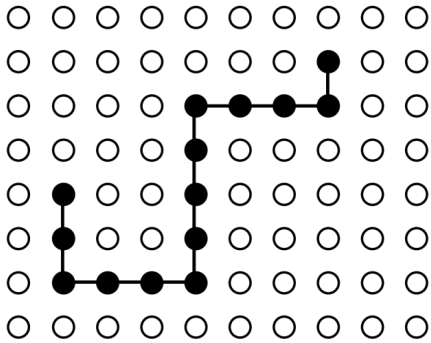

Figure 2.10 Lattice of a binary mixture: polymer (black connected dots) and low molar mass solvent (open circles).[55]

Considering the different arrangements of the polymer in the lattice leads to an entropy of mixing in the form of:

$$\frac{\Delta S_{mix}}{N} = -R\left(v_1 \ln v_1 + \frac{v_2}{x} \ln v_2 \right) \tag{2.2}$$

where v_1 and v_2 are the volume fractions of solvent and polymer, respectively; x is the number of lattice positions occupied by each polymer molecule;

$N = N_1 + xN_2$, with N_1 and N_2 the number of moles of solvent and polymer, respectively; and R is the ideal gas constant.

Enthalpy translates the interaction energies between solvent molecules and solute segments and is given by:

$$\frac{\Delta H_{mix}}{N} = RT\chi_{12}v_1v_2 \tag{2.3}$$

where χ_{12} is the Flory-Huggins (or interaction) parameter§§, which provides a measure of the goodness of the solvent for a particular polymer and is defined as:

$$\chi_{12} = \frac{z\Delta\omega_{12}}{RT} \tag{2.4}$$

with $\Delta\omega_{12}$ as the interchange energy (the energy associated to the formation of a polymer-solvent contact) and z as the coordination number of the lattice.

Finally, by combining equations 2.1, 2.2 and 2.3, the free energy of mixing for polymer solutions according to the Flory-Huggins theory is written as:

$$\frac{\Delta G_{mix}}{N} = RT\left(v_1 \ln v_1 + \frac{v_2}{x}\ln v_2 + \chi_{12}v_1v_2\right) \tag{2.5}$$

The first two terms refer to an entropic contribution arising from different arrangements of the polymer chains in the solvent. Possible entropy contribution from specific interactions between neighbouring solvent and polymer molecules is neglected and considered to influence enthalpy alone –

§§ The interaction parameter is a measure of the strength of the interaction between components, and is given by the change in energy that occurs when a molecule of material 1 is taken from a pristine environment and put into another environment where it is completely surrounded by molecules of material 2.[58]

which is given by the last term of the equation. It should be noted that for polymer/polymer blends ΔS_{mix} is positive and generally very small (due to the length and size of the polymer chains that hinder effective mixing), and so spontaneous mixing of such a system ($\Delta G_{mix} < 0$) is only possible when ΔH_{mix} is equally small or even negative.[55–57]

With equation (2.5) it is now possible to plot the free energy of mixing (ΔG_{mix}) against the composition for a positive value of the interaction parameter ($\chi > 0$), as shown in figure 2.11.[58]

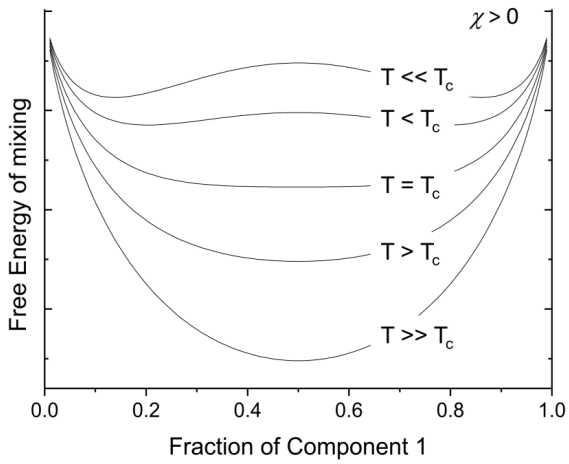

Figure 2.11 Free energy of mixing as a function of composition for several temperatures, when $\chi > 0$.

The shape of the curves of the free energy of mixing against composition give an account of the phase behaviour of the mixture: for temperatures above the critical temperature (T_c) the curves are concave with a single minimum; those below T_c show two minima and a local maximum. Analysing these curves, it is possible to see that for the simple concave curve, the solution will be miscible for all compositions – the free energy of mixing of the phase separated solution (which is given by the sum of the free energy of each of the phases weighed by

their volume fraction) will be higher than the free energy of the mixture. For $T < T_c$ there is a convex curve, the free energy of mixing is minimized when there is phase separation and so the mixture is unstable. In this case, the limiting compositions linking this two-phase region are those joined by a common tangent. These are called the coexisting compositions, or binodal points.

For curves with an unstable region, it is possible to identify two regions with positive and negative curvatures of the second derivative of the free energy function (see figure 2.12). The inflexion points are called spinodal points and

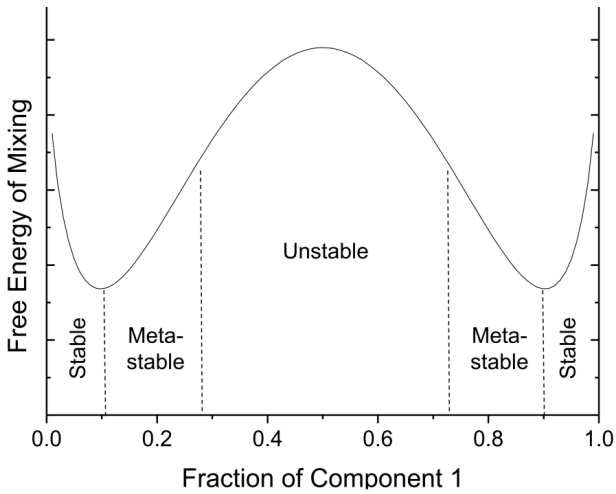

Figure 2.12 Free energy of mixing as a function of composition for a temperature below T_c.

define a border between a region of instability and a region of metastability. Where $\partial^2\left(\frac{\Delta G_{mix}}{N}\right)\Big/\partial v_1^2 < 0$, the system is unstable with respect to small fluctuations in composition, immediately phase separating; where $\partial^2\left(\frac{\Delta G_{mix}}{N}\right)\Big/\partial v_1^2 > 0$ an equally small composition fluctuation leads to an

increase of free energy and the system is then stable to these small fluctuations, although still globally unstable.

Plotting the same graph as a phase diagram (temperature vs composition) gives figure 2.13. The binodal and spinodal points are now binodal and spinodal curves, separating the stable, metastable and unstable regions.

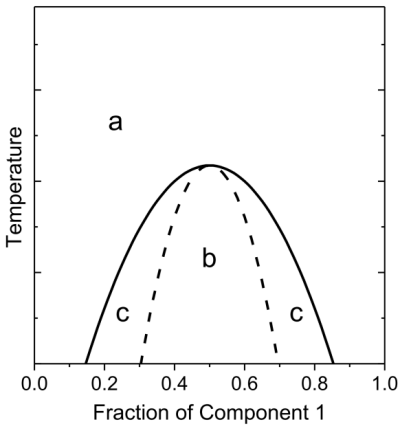

Figure 2.13 Phase diagram, correspondent to the graph in figure 2.12. In region **a** the mixture is stable and there is no demixing; in region **b** the mixture is unstable and will phase separate by spinodal decomposition; and in regions **c** the mixture is metastable and will demix if the minimum energy required for nucleation is overcome (phase separation by nucleation and growth).

There are two distinct mechanisms for phase separation. In the unstable region, the phase separation occurs by a continuous change in composition, with no energy barrier for nucleation of a new phase. This process is called spinodal decomposition and it happens by amplification of concentration fluctuations already present in the mixture at thermal equilibrium.[58,59] It is exemplified in figure 2.14. The resulting morphology is a random bicontinuous two-phase structure with a characteristic length scale, as depicted in figure 2.15a.

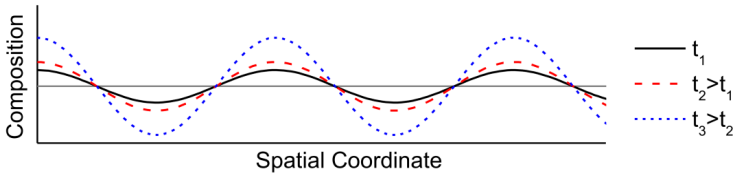

Figure 2.14 Variation of local composition over time.

In the metastable region, phase separation occurs by nucleation and growth. The blend is stable for small composition fluctuations and only after large fluctuations lead to the formation of a nucleus for another phase will this new phase be energetically favourable and grow. There is, in this case, an energy barrier for the formation of a new phase. After this is surpassed, the domains will grow driven by the reduction of interfacial area until an equilibrium composition is reached. The resulting morphology is characterized by isolated domains, as illustrated in figure 2.15b.

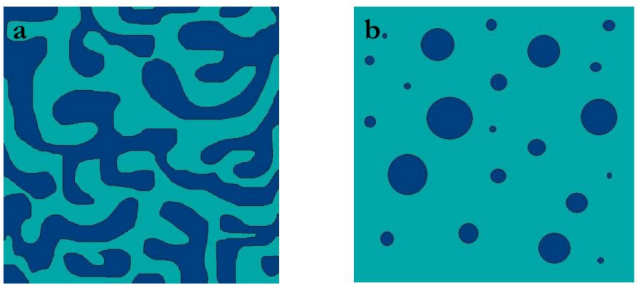

Figure 2.15 Resulting morphologies of phase separation via (a) spinodal composition and (b) nucleation and growth.[60]

The Flory-Huggins theory can be generalized to multicomponent systems, such as ternary systems of polymer/molecule/solvent of which polymer/fullerene solutions, from which photoactive layers for solar cells are prepared, are an example. Equation 2.5 is similar for these systems, but with three independent interaction parameters to account for all the different interacting pairs.[61] A phase diagram for ternary systems will be an equilateral triangle with three

composition axis, as illustrated in figure 2.16. The apex of the coexistence curve represents the critical concentration. The binodal and spinodal curves can be read as for a two-component diagram.

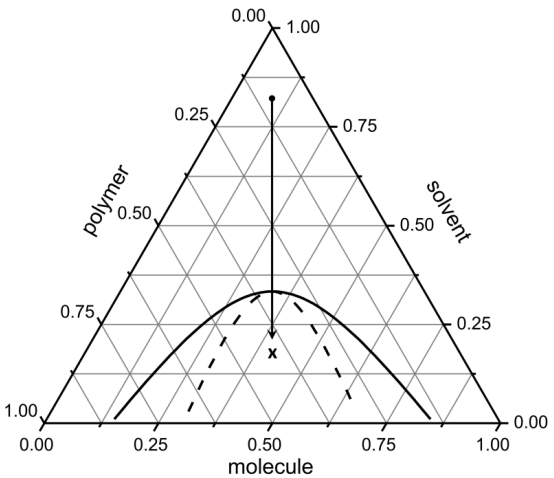

Figure 2.16 Example of a ternary phase diagram, for a polymer/molecule/solvent system. As the solvent evaporates, the system quenches into the unstable region, marked **x** in the diagram.

Phase separation in ternary systems of polymer/molecule/solvent is of great importance due to its direct influence in film morphology, and consequently in polymer photovoltaic devices performance. The temperature and concentration dependence of phase separation may be viewed as a very useful tool in tuning device performance since it enables the control of interfaces and pathways in the film. Phase separation mechanisms in blend solutions are also influenced by interaction phenomena at the free surface and at the interface with the substrate. These may induce phase separation in a direction normal to the substrate (vertical phase separation), triggered by the surface energy of the blend components.[59,62] The component with the lowest surface energy will preferentially migrate to the free surface in order to minimize the overall energy of the resulting film surface and phase separation will be directed from the free surface. Similarly, substrate-directed phase separation may also occur due to a

strong preference of one of the blend components for the substrate, influencing the wetting behaviour of the blend.[54,63,64] For blends in the unstable region, demixing by spinodal decomposition will be surface-directed in the vicinity of an interface whereas it is a random process in the bulk. In this way, stratified phases may be formed in the early stages of film formation that can either be frozen in by rapid quenching or break up into lateral domains when given more time (slower drying) due to interfacial instabilities.[65–70]

2.5 Stability issues in polymer photovoltaics

The improvement of the efficiency of organic solar cells to values in excess of 10%[4,5] have made viable commercialization of OPV a more likely scenario and interest in resolving stability and lifetime issues has increased.[71–75] Recently, efforts put forth during the first three International Summits on OPV Stability (ISOS) to develop protocols for testing and reporting stability and operational lifetimes culminated in the establishment of standard guidelines.[75,76]

Due to the complexity of OPV device structures, there are numerous possible degradation pathways and failure modes, making it particularly challenging to study and to control stability.[71] Cause diagnostic is further complicated by the fact that many processes are interdependent and multicausual. A common strategy to overcome this difficulty is the study of incomplete cells as model systems, combined with spectral response and current-voltage measurements on complete devices and other characterization techniques.[72]

There are three main stages at which OPV stability is important: fabrication, storage (shelf life), and operation (device lifetime). Each stage has its own particularities, and different degradation pathways can dominate. Degradation can be chemical, physical and/or mechanical in nature, and occurs at each structural layer and interface of the device. A brief account of degradation

issues in the **active layer**, in **contacts and interlayers**, and in the **encapsulation** is given below. Module degradation is also critical, but will not be addressed here.

Active layer

Degradation of the active layer can occur by chemical modification of its components or by changes in donor/acceptor morphology. Photochemical reactions that modify conjugation and ordering, and hence affect the material's optical and electrical properties, are a major concern since light exposure cannot be avoided. Photooxidation, leading to disrupted π-systems and/or chain scission, is believed to be the dominant degradation mechanism.[75] Preventing oxygen and moist diffusion into solar devices, for example by encapsulation, is crucial to minimize these degradation processes. The conjugated polymers used in solar cell research nowadays have been developed mainly for increased efficiency but turned out to have a higher intrinsic photochemical stability than the earlier polymers (e.g. poly-phenylenevinylene, PPV).[73] They are nevertheless still vulnerable to photodegradation. Manceau et al. have recently attempted to establish a rule of thumb for developing stable systems by analysing structure-stability relationships in a variety of polymers.[77] They presented a stability ranking of the most commonly used monomers in the field that could be used as a rough guide for the synthesis of more stable polymers. Furthermore, they concluded that keeping the amount of side groups as low as possible, regardless of their chemical nature, improves stability. Attempts at improving polymer stability have been made by removing said side chains by thermo-cleavage mechanisms after film processing from solution.[78] Interestingly, the photostability of polymer semiconductors is increased in blends with PCBM.[79–81] The reason for this has not been completely understood, but is thought to be related to quenching of the polymer's excited state. Fullerene-based molecules themselves are also susceptible to chemical degradation, in particular photooxidation.[80] While C_{60} and PCBM have been the acceptor materials of choice in the field of OPV, very little attention has been

given to studying their stability in this context. Recent studies show that degraded fullerene-derivatives can have a strong effect on photovoltaic performance.[80,82] Elucidating the mechanisms for degradation in fullerenes and fullerene-derivatives used in solar cells and establishing design rules for the development of more stable acceptors will contribute to increasing the general photostability of the devices.

An optimized active layer morphology is hard to achieve (see section 2.4) and it is generally not thermodynamically stable. This means that it can evolve further with time, even at ambient temperature, lowering device performance. Several strategies to stabilize D/A morphology have been attempted. These include modifying donor and/or acceptor in order to minimize diffusion rates[83] or crystallization processes;[84,85] photo or thermal cross-linking, to stabilize optimum nanomorphology;[86–91] and the use of compatibilizers, which suppress phase separation.[92–95]

Contacts and interlayers

Top electrodes in traditional device architectures are vacuum deposited low work function metals, normally aluminium or calcium. Thermal evaporation of the metal can generate metal boundaries and pinholes through which water and oxygen can diffuse.[74] Unfortunately, metals with low work function oxidize easily. This may lead to the formation of an electrically insulating layer of metal oxide at the interface with the active materials, hindering electron collection. Inverted solar cell geometries use higher work function metals as top electrodes, commonly silver, which are less reactive and can be deposited from solution.[74] The use of an interfacial layer, e.g. LiF,[45] between the photoactive layer and the metal electrode (both in traditional and in inverted architectures) has been shown to enhance performance of solar devices and improve stability. Some concerns over LiF dissociation upon thermal annealing and subsequent migration of the Li ion have nevertheless been raised.[73,96] Lately, polymeric and

molecular interlayers have emerged as a promising alternative, but their degradation pathways still remain to be studied.[73,75]

Stability issues with the transparent ITO bottom electrode and the PEDOT:PSS interfacial layer are also known to occur. The main problem with ITO is that it is susceptible to chemical etching and migration of indium throughout the device may occur as a result.[97] The poor mechanical properties of ITO are also a factor, in particular when considering applications that call for flexible, bendable substrates that can induce crack formation in the electrode. Possible substitute materials, such as carbon nanotubes,[98,99] graphene,[100] or other oxides are being considered. ITO's sensitivity to air and moisture makes the combination with PEDOT:PSS an unfortunate one since this ionic polymer is commonly found as a water-based dispersion. Even after the standard thermal treatment to eliminate water residue, the hygroscopic PSS easily takes up moisture from the atmosphere contributing to increased degradation of the ITO electrode and performance of devices.[101] Moreover, the acidic nature of PEDOT:PSS induces the ITO etching mechanism mentioned above.[102,103] Other issues with PSS include formation of insulating patches at the interface with the active layer.[104]

Encapsulation

Encapsulation of OPV devices is required in order to increase their mechanical stability and scratch resistance and, most importantly, to slow down oxygen and moisture ingress – which are the main triggers for OPV degradation. In order to achieve the necessary low transmission rates of oxygen and water, adequate encapsulation in needed.[72] Full glass encapsulation or a combination of a glass front and a metal back plate work effectively, but they lack mechanical flexibility. Alternative barrier films must have oxygen- and water-impermeability, thermal stability, chemical resistance and a high optical transparency comparable to those of glass, but they should also offer the mechanical properties that allow the fabrication of flexible OPV through easy

lamination processing. The use of polymeric materials as barriers is not suitable for OPV encapsulation, as even the most up-to-date films used in food and drug-packaging have too high transmission rates. Promising organic/inorganic multilayer films are being developed as an alternative.[72]

Chapter 3

Materials and sample preparation

3.1 Materials

Donor materials

The work of this thesis was done with four different conjugated polymers, all alternating polyfluorenes (APFO). APFOs have alternating fluorene units and donor-acceptor-donor (D-A-D) segments forming the backbone of the polymer.[23,105–107] In this way, it is possible to narrow the energy bandgap of the material – the alternating electron-donating and electron-accepting units increase the double-bond character of the single-bonds in the polymer – and improve the spectral overlap with the solar spectrum.[16,108–110] By controlling the polar character of the side chains, the miscibillity between polymer and fullerene, and thus the BHJ morphology, can be tuned.[111]

APFO-3

The APFO-3 polymer (poly[(9,9-dioctylfluorenyl-2,7-diyl)-co-5,5-(4',7'-di-2-thienyl-2',1',3'-benzothiadiazole], also referred to in the literature as LBPF5, PFDTBT, F8DTBT or PFO-DBT) was used in the work published in **paper I**. The synthesis[112] was done at the Department of Chemical and Biological Engineering, Chalmers University of Technology – Sweden. APFO-3 was used as received. Its chemical structure is shown in figure 3.1. The batch used had a M_n ~ 8 000 and M_w ~ 14 000, number-average and weight-average molecular

weights respectively. The electrochemically determined values for the HOMO and the LUMO levels of this polymer are -5.8 eV and -3.5 eV, respectively.[113] The density of the polymer is estimated to be 1 g/cm^3.

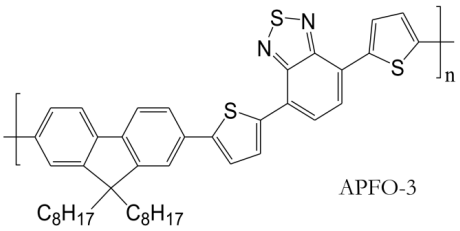

Figure 3.1. Chemical structure of the polymer APFO-3.

APFO-Green11 to 13

In **papers II and III**, a set of new copolymers (APFO-Green11, APFO-Green12 and APFO-Green13) designed for tailoring the chemical compatibility of the donor and the acceptor materials was studied. Their chemical structure is presented in figure 3.2. These copolymers were synthesized with varying fractions of a phenolic monomer in which the hexoxy side chains on the pyrazine unit in the D-A-D segment have been replaced by an hydroxyl group. This modified monomer has the potential of forming hydrogen bonds with the side chain of PCBM. APFO-Green11 was synthesized with no phenolic monomer; APFO-Green12 and APFO-Green13 were polymerized with 5% and 10% of the phenolic monomer, respectively. The polymers were synthesized at the Department of Chemical and Biological Engineering, Chalmers University of Technology – Sweden and used as received. The general synthethic route can be found in reference 111. Molecular weights and polydispersity indices (PDI) were determined by matrix-assisted laser desorption/ionization – time-of-flight (MALDI-TOF) mass spectrometry and size exclusion chromatography (SEC), using polystyrene standards and 1,2,4-trichlorobenzene (135 °C) as the solvent. The number-average molecular weights, M_n, obtained from SEC were 23 000, 26 000 and 17 000 for APFO-

Green11, 12 and 13, respectively. From MALDI-TOF, M_n values were in the range of 4 000 – 5 500 for all three polymers. The weight-average molecular weights, M_w, were 317 000, 244 000 and 62 000 for APFO-Green11, APFO-Green12 and APFO-Green13, respectively. All polymers have rather high PDI values, though this is most pronounced for APFO-Green11 and 12 (PDI of 14 and 12, respectively, compared to a PDI of 4 for APFO-Green13). The differing M_n are likely due to the high PDI values and the fact that in MALDI-TOF measurements low molecular weight fractions tend to be overestimated. The density of the polymers is estimated to be 1 g/cm^3.

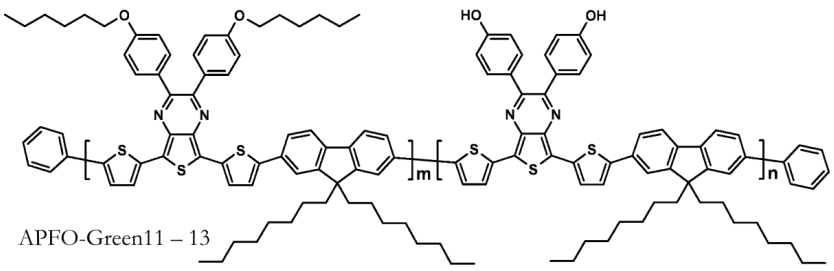

Figure 3.2. General chemical structure of the polyfluorene copolymers APFO-Green11 (100:0), APFO-Green12 (95:5) and APFO-Green13 (90:10).

Acceptor materials

Both the substituted fullerene PCBM, (**papers I to V**), and its pentadeuterated form, d5-PCBM (**paper II**) were used in this work. Their chemical structures are shown in figure 3.3. They were purchased from Solenne B.V. (Netherlands) and used as received. The batches were of scientific grade (>99.5% purity). The HOMO and LUMO levels mentioned in the literature vary because of different measurement techniques.[35] Values of -5.9 eV for the HOMO and of -3.73 eV for the LUMO of PCBM have been estimated from cyclic voltammetry.[114] Reported density values[103,115] range from 1.3 to 1.5 g/cm^3. In **papers I** and **III** the value of 1.5 g/cm^3 was used.

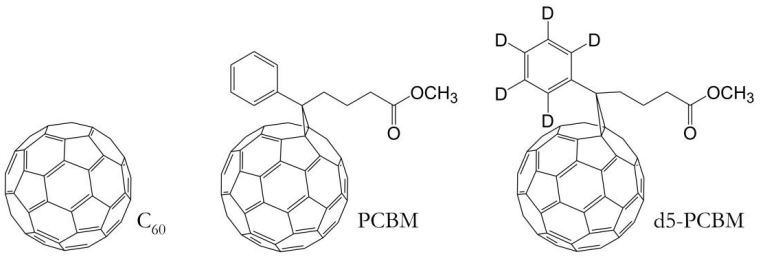

Figure 3.3. Chemical structures of buckminsterfullerene, and the fullerene derivatives PCBM and d5-PCBM.

C_{60} (**paper V**) with 99.98% purity was purchased from Term, (USA) and used as received. It has a HOMO level at -6.03 eV and a LUMO level at -3.82 eV, estimated from cyclic voltammetry.[114]

3.2 Sample preparation

3.2.1 Thin film preparation

The majority of the thin films studied in this work were prepared by spin-coating from halogenated solutions. C_{60} was deposited by thermal evaporation in high vacuum. Details can be found in the experimental section of the appended papers. A brief description of film formation by spin-coating follows.

Spin-coating

Spin-coating (or spin casting) is one of the more popular methods for applying thin uniform films onto flat surfaces. It is used routinely in polymer photovoltaic research, due to its ease of use and relative low cost, although it is not particularly suited for large-scale film processing.[116] Figure 3.4 shows an image of a spin-coater. In spin-coating, a solution drop of the coating material dissolved in an appropriate solvent is dispensed onto the substrate surface,

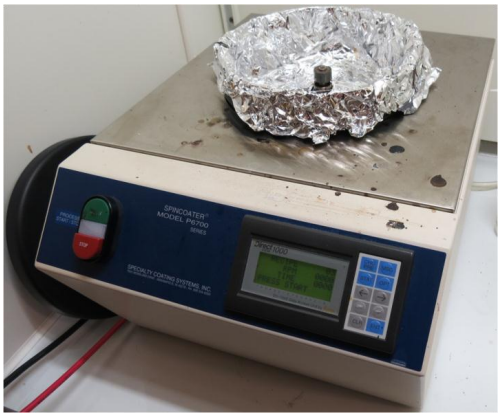

Figure 3.4 Spin coater from Specialty Coatings Systems, Inc. (USA).

which is made to rotate at large velocity (typically around 1000 – 3000 rpm). The spinning motion spreads out the solution and, as the solvent evaporates away, a thin film of coating is left on the surface.

The basic spin-coating process can be divided into three stages[117], as illustrated in figure 3.5.[118]

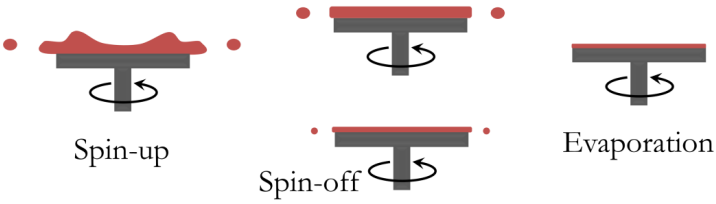

Figure 3.5 The three stages of spin-coating: spin-up, spin-off and evaporation. (Adapted from reference 118)

The first stage starts as the drop of solution is deposited on the substrate and there is an acceleration of the spin speed to the final desired value. During this stage, most of the fluid is flung off the surface, leaving a thin enough layer that co-rotates with the substrate. The second stage is characterized by fluid viscous forces dominating fluid thinning and determines the thickness and uniformity

of the final film. The third stage begins when fluid viscosity is so high that the net fluid flow becomes negligible and solvent evaporation is the major process of the coating thinning behaviour. At this point it is possible to say that the solute is frozen on the surface, held still by high viscosity, in a non-equilibrium state.[117,119]

In general, higher spin speeds (ω) generate thinner films, in a relation ruled by equation 3.1, where h_f is the film thickness, $x_{1,0}$ represents the initial polymer weight fraction and k is a constant dependent on the polymer-solvent system.

$$h_f = k x_{1,0} \omega^{-\beta} \tag{3.1}$$

The value of β has been found to be 0.5 for most materials used for coating, although some deviations occur. Recently, a β of 0.4 was calculated for the conjugated polymer P3HT (poly(3-hexylthiophene)), although the theoretical value of 0.5 was predicted for higher molecular weight samples, which correspond to higher viscosities.[120,121]

As the spin speed increases, there is an increase in the radial flow which, along with solvent evaporation, leads to film thinning. These are the two balancing forces at work in stages two and three: centrifugal and viscous forces. Because the radial flow depends on the balance between viscous forces resisting the flow and centrifugal forces created by the spinning, viscosity of the polymer-solvent system plays an important role in the final film thickness and, consequently, so does solution concentration.

The quality of the film is therefore dependent on spin speed and concentration, but also on solvent properties such as vapour pressure that determine how long the two latter stages last. Solubility of the polymer in the solvent is then of major importance as well. It is especially important in cases of coating solutions

of two components in a common solvent, since different solubility of the two components in the solvent leads to different evaporation times that may be reflected on non-uniformity of film thickness with possible domain formation.[54,122]

3.2.2 Device fabrication

Devices were prepared on 2×2 cm^2 glass slides. The geometry used (see figure 3.6) yields four devices per substrate, each with an active area of 2×2 mm^2. Details of device fabrication can be found in the experimental section of paper III.

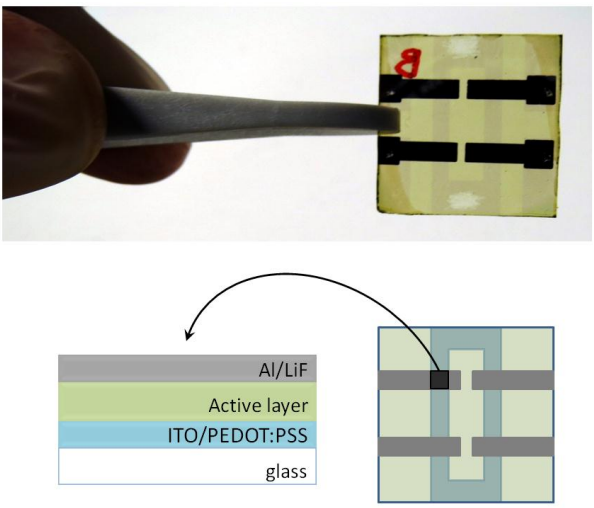

Figure 3.6 One of the substrates (top) and the corresponding schematic diagrams (bottom). One of the four solar cell pixels is highlighted in dark gray in the top view diagram (bottom right). A side view illustration of the different layers in each pixel is given at the bottom left (arbitrary layer thicknesses).

Chapter 4

Characterization techniques

The morphology of the active layer influences the performance of BHJ polymer solar cells to a large extent. The steady efficiency improvement shown in several systems after optimization of the film preparation conditions in order to yield more favourable film organizations[123–126] has triggered the interest of the scientific community in the influence of morphology on the physical properties of the active layer and on the device performance. Although there is already a considerable amount of accumulated knowledge on structure-property relationships,[59,127–135] tailoring the film morphology to meet an optimized performance still remains a challenge. In particular, knowledge about the three-dimensional organization of the film at different scales and on the local organization at the electrode interfaces would be invaluable for the development of more efficient organic photovoltaic devices.

The complexity of the problem is related not only to the wide range of parameters influencing final film morphology but also to the lack of appropriate analysis tools that allow for a full nanoscale film characterization of the resulting morphologies when these parameters are systematically altered.

Morphological studies of BHJs focus both on lateral and on vertical characterization. Commonly used microscopy techniques include Atomic Force Microscopy (AFM); Scanning Electron Microscopy (SEM);[136] Scanning Transmission X-ray Microscopy (STXM);[137] and Transmission Electron

Microscopy (TEM).[138–141] Characterization of the free and buried surface is also done with e.g. X-ray Photoelectron Spectroscopy (XPS)[142,143] and Ultraviolet Photoelectron Spectroscopy (UPS).[96] Vertical concentration gradients can be probed by use of such techniques as variable-angle spectroscopic ellipsometry (VASE);[144] neutron reflectivity;[115] dynamic Secondary Ion Mass Spectrometry (dSIMS);[145–147] and Rutherford Backscattering Spectrometry (RBS). More recently, electron tomography has been used to form 3D images of BHJs by combining a series of 2D projections by TEM taken at different sample tilts.[127,148–151] Synchrotron-based characterization methods like near-edge X-ray absorption fine structure (NEXAFS) spectroscopy have been used lately for characterization of the chemical composition of both the top and the buried interface of photoactive layers.[152–155]

The characterization techniques used for the work presented in this thesis are described below.

4.1 Atomic force microscopy

Atomic force microscopy was developed in 1986 by Binnig and co-workers.[156] By combining scanning tunnelling microscopy with stylus profilometry principles, they introduced a new scanning probe technique for high-resolution surface topography. It is based on the detection of forces between a sharp tip and the sample surface, information which is used to create a topographical image of the sample.

Two basic analysis modes of AFM are the contact mode and the intermittent (or tapping) mode. While sweeping the tip over the surface, tip response is monitored and corrected to a constant value (of deflection, in contact mode; and amplitude, in tapping mode) by changing the tip-sample distance (i.e. z-position). Adjustments of z-position are done via a feedback control unit and a

piezoelectric system. These corrections provide the data that is then translated into a 3D image of the sample surface. Figure 4.1 shows a schematic diagram of the system.[157]

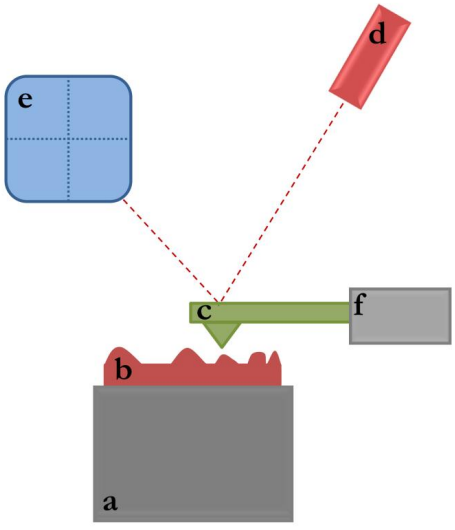

Figure 4.1 The main components of AFM: *(a)* piezoelectric sample holder; *(b)* sample;*(c)* cantilever and tip; *(d)* laser; *(e)* position-sensitive photodiode detector;*(f)* tip holder, with piezo stack for use in tapping mode.

4.1.1 Contact mode atomic force microscopy

In contact mode the tip is in contact with the sample and the detector measures the cantilever's deflection as the tip is rastered across the sample surface. This deflection is kept constant by adjusting the z-position through a feedback loop. The result is a topographical image of the surface. In soft samples, there is a danger of image distortion and even sample damage when contact mode is used, due to possible high lateral forces arising from the scanning motion. These can, however, give extra information in the case of hard samples, as tip-sample nanoscale frictional forces can be monitored by detecting the torsion of the cantilever.

4.1.2 Tapping mode atomic force microscopy

In tapping mode AFM (TM-AFM) the cantilever is made to oscillate near or at its resonance frequency, tapping the surface during the scan. It is the oscillation amplitude of the tip oscillation that is kept constant by adjusting the z-position. The resonance frequency of the oscillation is also affected by the interaction with the surface. Shifts in this oscillation frequency provide additional information and the phase lag between the drive frequency and the cantilever oscillation frequency can be recorded simultaneously with topographical data. Changes in the phase are generally interpreted as variations in the tip-sample interaction due to compositional changes of the surface (which may result in local variations in adhesion, friction, viscoelasticity and others).[158] With TM-AFM there is less damage to soft surfaces and better lateral resolution. For these reasons, it is the preferred mode when imaging polymer films, even yielding phase contrast images in highly phase-separated blends.

4.1.3 Instrumentation

A Nanoscope IIIa Multimode atomic force microscope (figure 4.2) from Veeco Metrology Group was used in both Tapping Mode and Contact Mode – for surface analysis and film thickness measurements, respectively. TM-AFM was conducted using a silicon cantilever (OMCL-AC160TS series, from Olympus) with a spring constant of 42 Nm^{-1}, a resonance frequency of 300 kHz and a tip radius of less than 10 nm. The tip used for contact mode was a triangle shape gold-coated silicon nitride cantilever with a spring constant of 0.09 Nm^{-1} (OMCL-TR series, from Olympus).

Figure 4.2 Nanoscope IIIa Multimode atomic force microscope from Veeco Metrology Group.

4.2 Dynamic secondary ion mass spectrometry

Dynamic secondary ion mass spectrometry is one of the possible analytical modes in secondary ion mass spectrometry. In this technique, a sample is bombarded with a primary ion beam and the emitted secondary ions are analysed with a mass spectrometer. In the dynamic mode, the sample is gradually sputtered away while being continuously analysed. This yields chemical information as a function of depth which can be presented in a depth profile.

As the bombarding ion beam, of a few keV, hits the sample surface, energy is transferred from the incident ions to the sample and mono and polyatomic particles (positively, negatively and neutrally charged), along with re-sputtered primary ions, electrons and photons, are produced. The formation of these

secondary ions originating from the sample can be described by the collision model: the primary ion beam energy is passed on to target atoms in a series of two-body collisions; the target atoms that recoil back through the sample surface are the sputtered material that will be analysed.[159] A mass spectrometer identifies these secondary ions based on their mass to charge ratio.

Due to the large variation in detection sensitivity for different elements, the ion yields (i.e. the fraction of ionized sputtered material) can vary by several orders of magnitude, which affects elemental sensitivity and detection limits. Therefore, direct correspondence between signal intensity (ion counts) and concentration is difficult. Compounding this difficulty is the fact that the quantitative detection of each secondary ion is also dependent on instrumentation and measuring parameters, such as primary ion beam density, elemental surface concentration, probability that the ion survives in its ionized state until detection and transmission of the mass spectrometer for that specific element.[159–161]

The conversion of the sputter time axis into depth measured from the surface is more straightforward. It can be done by making an independent measurement of the final depth of the sputtered crater and dividing it by the total sputter time, which gives an average sputter rate. Alternatively, the sputter yield can be measured for a pure element or smooth amorphous sample and later used to calculate the relation between sputtering time and depth scales. However, in crystalline and/or compound samples the elemental sputter yields can be extremely affected and deviate significantly from the ones calculated for the reference sample.[161]

4.2.1 Instrumentation

dSIMS depth profiles were taken at the Macromolecular Nanofilms for Electronics and Biotechnology group of Prof. Andrzej Budkowski (Jagiellonian

University, Poland). The system was a VSW (UK) apparatus equipped with a liquid metal ion gun (FEI Company, USA). The samples were gradually sputtered with a Ga^+ primary ion beam of 5 keV, scanning over a 100 μm×100 μm region. Secondary ions, with mass to charge ratios (m/q) of 14, 24, 26, 28 and 32, were collected from the central part of the sputtered region (50%) and analysed with a quadrupole mass spectrometer (Balzers, Liechtenstein). The depth resolution of the resulting profiles was 10 nm.[147,162]

4.3 Near-edge X-ray absorption fine structure spectroscopy

NEXAFS probes the unoccupied electronic states of a sample's molecular orbitals. A monochromatic X-ray beam is incident on the sample. By sweeping the photon energy of the incident radiation across a specific absorption edge, an X-ray absorption spectrum can be recorded. Each spectrum is composed of characteristic absorption resonance peaks generated from core electron transitions. An incident photon with an energy above the absorption edge excites a core level electron into an unoccupied energy level. This excited state is unstable and the core level hole is filled via the relaxation of an electron from a higher state, accompanied by the emission of an Auger electron or a fluorescent photon.[163] This process is shown schematically in figure 4.3.

The probability for photon absorption can be monitored in different ways. Directly, by measuring the photon transmission through the sample, or indirectly, by measuring the emission of secondary electrons (electron yield methods) or of energetic photons (fluorescence yield). Using different energy discrimination regimes in the electron yield measurement, the surface sensitivity of the detection method can be altered. The least surface-sensitive method is the total electron yield (TEY) mode where all the electrons leaving the sample

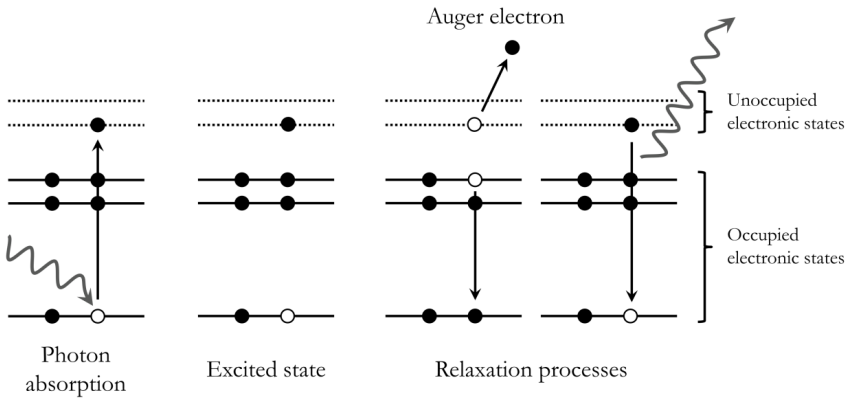

Figure 4.3 The photoabsorption and relaxation processes in a NEXAFS experiment.[164]

are counted, generally by measuring the sample drain current. Partial electron yield (PEY) mode excludes slow electrons (multiple scattered and secondary electrons) by applying a retarding voltage to the entrance of the electron detector. This voltage can be chosen to select electrons from different kinetic energy regimes. It is also possible to include only the electrons whose kinetic energy lies within a specific Auger transition energy, in which case the Auger electron yield is measured (AEY). The surface sensitivity of these detection methods increases from transmission, through fluorescence, TEY, PEY, to AEY – which is the most surface sensitive detection mode.[163,164]

NEXAFS spectra are element-specific and are generally taken within a 30 eV energy window above the absorption edge. Lighter elements, like carbon, nitrogen and oxygen, have rich NEXAFS spectral fingerprints, which makes this method especially suited for the study of organic molecules and polymers. The resonance peaks corresponding to transitions to low-lying π^* and σ^* anti-bonding orbitals are generally well separated in energy and are highly dependent on the bonding arrangements of the excited sample atoms. This makes NEXAFS an excellent tool for chemical analysis of polymeric thin film surfaces.[165–167]

4.3.1 Molecular orientation from angle-resolved spectra

The polarized nature of X-rays from a synchrotron source yields additional information about the orientation of the molecules because the resonance peak intensity is a function of the alignment of the beam's electric field vector with the final state orbital direction (see figure 4.4). Therefore, angle-resolved measurements are another important feature of the NEXAFS technique and can help resolve the bonding and orientation of the molecules in the probed region. These are normally done by systematically changing the angle of the sample with respect to the incident beam, ranging from 20° to 90° (measured from the sample surface), and the resulting peak intensities will vary accordingly in oriented systems.

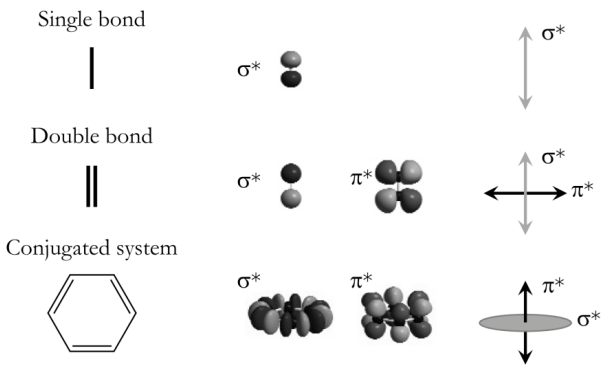

Figure 4.4 Schematic representation of directional resonances for single bond; double bond; and conjugated system.[168,169]

Peak intensities (*I*) of vector orbitals are given by

$$I = A\left\{\frac{P}{3}\left[1+\frac{1}{2}\left(3\cos^2\theta-1\right)\left(3\cos^2\alpha-1\right)\right]+\frac{(P-1)}{2}\sin^2\alpha\right\} \qquad (4.1)$$

where A is a cross-sectional constant, P is the polarization factor of the beamline, θ is the angle of the incident radiation with respect to the sample surface and α the angle of the vector orbital relative to the sample normal.[169]

From plots of I vs $\cos^2\theta$ or I vs $\sin^2\theta$, A and α can be determined. However, angle α will be a measure of the average orientation of the vector orbital in the sample volume and not a strict orientation angle for every molecule in that volume – with the exception of extremely ordered materials, e.g. self-assembled monolayers. In samples where the molecular orientation is not high, as is the case in polymer films, it is only indicative of an orientation tendency.

Instead of using the angle α, it is possible to express the orientation tendency in a sample in terms of the dichroic ratio, R:

$$R = \frac{(I_{90^\circ} - I_{0^\circ})}{(I_{90^\circ} + I_{0^\circ})} \tag{4.2}$$

The intensities at perpendicular incidence, I_{90°, and at grazing incidence, I_{0°, can be extrapolated from the linear fit of the peak intensity dependence on $\sin^2\theta$ or $\cos^2\theta$. For perfectly polarized incoming light ($P = 1$), R can take values from 1, for a perfectly parallel orientation of the orbital vectors relative to the surface of the film, to -1, for orbital vectors that are oriented perfectly perpendicular to the surface. An R value of 0 (zero) indicates a random orientation of the molecules or a strict 54.7° orientation measured from the surface (the so-called magic angle). Intensity dependence on the angle of incidence is greater in orientations nearly parallel or perpendicular to the surface normal, and zero at the magic angle.[163,170]

4.3.2 Instrumentation

The NEXAFS measurements were carried out in the front chamber of beamline D1011 (see figure 4.5) of the synchrotron storage ring MAX II at MAX-lab, in Lund, Sweden. NEXAFS spectroscopy was used in both partial and total electron yield modes to probe the near-surface region of the polymer blend films at different depths. Linearly polarized X-rays with a polarization degree of about 96 to 99% were used. TEY and PEY NEXAFS spectra at the C1s absorption edge were collected simultaneously, for each incident angle (θ_{inc} measured from the sample surface). PEY spectra were collected using an applied entrance grid voltage of -150 V on the multi-channel plate (MCP) detector. The MCP detector was positioned below the sample, invariably perpendicular to it (see figure 4.6). TEY-NEXAFS spectra were collected by measuring the total current passing through the sample.

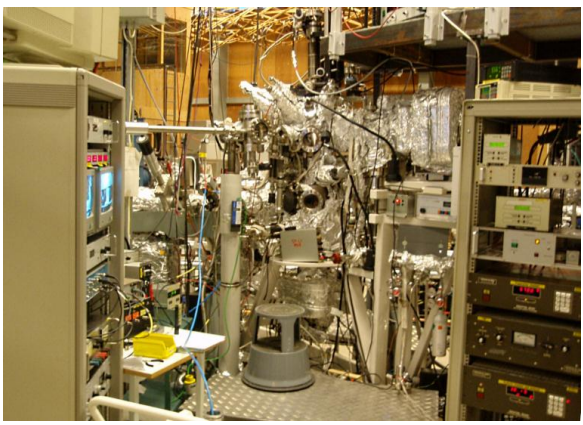

Figure 4.5 Front chamber of beamline D1011, at MAX-lab.

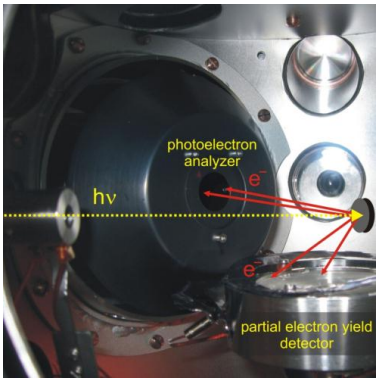

Figure 4.6 Overview of the analysis chamber in the front chamber of beamline D1011, highlighting the geometry of the incoming radiation and detection methods relative to sample position.
[source: https://www.maxlab.lu.se/node/458]

The raw spectral data were divided by the corresponding spectrum of a gold film on mica, sputter-cleaned *in-situ*, to correct for any X-ray absorption in the instrument, and subsequently normalized in the high photon energy region.[163,164] The energy calibration was done by using the σ* peak of highly oriented pyrolytic graphite (HOPG).[171] Further details can be found in the appended papers.

4.4 Photoemission spectroscopy

Photoemission spectroscopy is one of the most widely used techniques in surface analysis of unoccupied states. It is based on the photoelectric effect,[172,173] with photoelectrons being emitted as a result of the interaction of incident mono-energetic photons and the sample. The measured energy of the emitted photoelectrons, $E_{\text{kin,meas.}}$, is given by:[159,174]

$$E_{kin,meas.} = h\nu - E_{bin} - \phi_{spec} \tag{4.3}$$

where $h\nu$ is the energy of the incoming photon, E_{bin} is the electron binding energy in the solid, relative to the Fermi level, and ϕ_{spec} is the work function of the spectrometer.*** This equation is valid for photoelectrons that have suffered no energy losses, i.e. elastic photoemission. Although the radiation used in photoemission spectroscopy has a penetration depth of many microns, the probability that an excited electron will leave the sample with its original energy is low. The strong interaction of the photoelectron with the rest of the solid limits the distance that it can travel before it undergoes inelastic scattering (mean free path, λ). Thus this technique has a high surface sensitivity. Describing the depth origin of these electrons is crucial for a correct analysis; however this is a complex process, none the least for organic compounds.[175] The dependence of λ on the kinetic energy of the emitted electrons has been compiled for a collection of materials (see figure 4.7), which shows a universal behaviour independent of the material.[176] For energies ranging from 100 to 1000 eV (typical for studies of organic compounds), the mean free path extends only to a few nanometers (i.e. a few tens of Ångström).[159,174]

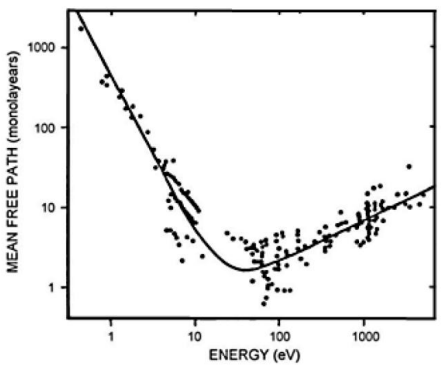

Figure 4.7 Mean free path of electrons in solid materials as a function of the electron energy above the Fermi level.[174]

*** The measured kinetic energy of the photoelectron ($E_{kin,meas.}$) differs from the kinetic energy of the photoelectron leaving the sample. Due to the difference in work functions of the sample and the spectrometer, alignment of the Fermi levels when electrical contact is made leads to the creation of a potential difference. In practice, the photoelectron is either accelerated or deccelerated towards the detector.

Photoelectron emission is studied by analysis of spectra of intensity (number of collected electrons) as a function of kinetic or binding energy (see figure 4.8), where emission either of tightly bound core electrons or of more weakly bound valence electrons is mapped. Less intense Auger emission peaks are also a part of the spectrum. The excitation and decay processes from which photoemission peaks originate are shown in figure 4.9.

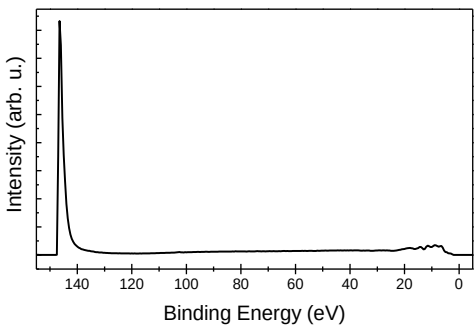

Figure 4.8 Widescan photoemission spectrum of an organic semiconductor material. It is possible to see the valence band (at low binding energies) and the secondary electron cut-off (at high binding energies).

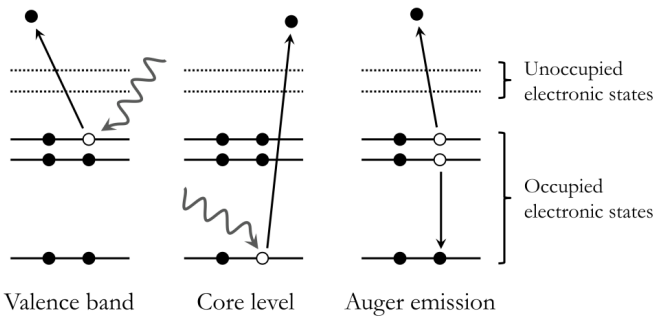

Figure 4.9 Excitation and decay processes in photoemission spectroscopy: an electron from the valence band is excited to the vacuum; a core level electron is excited to the vacuum; and, after a core level excitation, the remaining core hole is filled by the relaxation of an electron at a higher energy level, and the excess energy is released as an Auger electron.

The study of core levels is commonly referred to as X-ray photoelectron spectroscopy (XPS), as it uses radiation in the X-ray range, or electron spectroscopy for chemical analysis (ESCA), a term coined by Siegbahn and co-workers[177] and that directly reflects the close relation of the energy of the emitted photoelectrons with the chemical environment and the concentration of the emitting atoms in the sample. For probing valence levels, which will be discussed further in the next section, photons in the ultraviolet range are used and the technique is termed UV photoemission spectroscopy (UPS). The most common radiation sources are X-ray emission tubes with Mg or Al anodes for XPS measurements, and He gas discharge tubes for UPS measurements. Synchrotron radiation has come to play an increasingly important role in photoemission studies, as it yields a continuous spectrum covering photon energies ranging from the infrared to hard X-rays.[174]

4.4.1 Valence band spectra

Valence band spectra are the result of photoelectron emission from the delocalised bonding orbitals, mirroring the local density of filled states and serving as an electronic fingerprint of the sample surface. The electrons in these orbitals are characterized by low binding energies, typically in the 0 to 15 eV range. Because the orbitals that are probed are the ones directly involved in chemical bonding, valence band spectra are more sensitive to molecular structure than core level spectra and can be used for structural studies in combination with theoretical calculations.[159] When the high binding energy tail of the spectrum is measured, i.e. the low kinetic energy cutoff, the values of the work function and of the ionization potential of the sample can be determined. For work function calculations in a semiconductor, where the Fermi level is not measurable directly, it is necessary to ascertain the position of the zero binding energy by measuring on a clean metal sample, e.g. Au surface. For the ionization potential of organic compounds, it is the onset of the HOMO that is used.[178]

4.4.3 Instrumentation

The valence band spectroscopy experiments were performed in the front chamber of beamline D1011 of the synchrotron storage ring MAX II at MAX-lab, in Lund, Sweden. Electron collection was done with a SCIENTA SES200 electron energy analyzer (see figure 4.6), in normal emission geometry and at a photon energy of 150 eV. The position of the Fermi level was ascertained by measuring on a sample of Au on mica sputtered in-situ. No noticeable radiation damage was found during the measurements.

4.5 Ultraviolet-visible absorption spectroscopy

Ultraviolet-visible spectroscopy is routinely used for qualitative and quantitative studies of molecules with unsaturated bonds or heteroatoms, which undergo electronic transitions upon absorption in the ultraviolet and visible portion of the electromagnetic spectrum.

Absorption spectra is obtained by sweeping across the range of wavelengths of interest and measuring the intensity of light passing through the sample, I, compared to the intensity of light passing through an appropriate reference, I_0 (e.g. pure solvent in the case of solutions or clean substrate in the case of thin films). Absorbance is dependent on the number and the nature of the absorbing species, and can be generally described by the Lambert-Beer Law:[179]

$$A = -\log_{10}\left(I/I_0\right) = \varepsilon b C \tag{4.4}$$

where A is the absorbance; ε is the absorption coefficient, characteristic of each species; b is the length of the light path through the sample; and C is the concentration of the absorbing species.

The wavelength at which the absorption takes place yields information on the nature of the electronic transition, and it is affected by conjugation phenomena that may occur within the sample and by solvent interaction. Highly conjugated materials, with extended π-systems, can show red-shifted absorption and develop a fine structure reflecting different conformations of the system.

4.5.1 Instrumentation

Ultraviolet and visible absorption spectra in this work were obtained with a double-beam Shimadzu UV-Vis. spectrophotometer, model UV-2101 PC, with a wavelength accuracy of ± 0.3 nm. Spectra were collected at room temperature in the 300 – 900 nm wavelength range in steps of 1 nm.

4.6 Device characterization

4.6.1 Photocurrent-voltage characteristics

The electrical characterization of a solar cell is done by measuring the current density[†††] as a function of voltage (*J-V*) in the dark and under illumination. A typical *J-V* curve is shown in figure 4.10. The four main photovoltaic parameters that can be extracted from these curves are the short-circuit current density (J_{SC}), the open-circuit voltage (V_{OC}), the maximum power point, (*MPP*), and the fill factor (*FF*), marked in the *J-V* graph. In a simplified description, J_{SC} and V_{OC} can be related to different working regimes of a metal-insulator-metal (MIM) device, as can be seen in figure 4.11. It is in between regimes (a) and (b), i.e. quadrant IV, that the solar cell generates electrical power.

[†††] For convenience, the current density (which is the current divided by the active area) and not the current will be referred to. Current densities are generally preferred since they are independent of the size of the solar cell and are therefore more useful in comparisons.

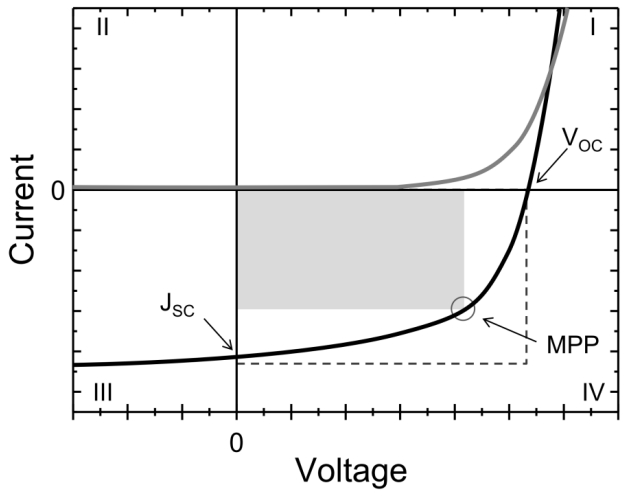

Figure 4.10 Typical current-voltage dependence of solar cell in the dark (gray line) and under illumination (black line). V_{OC}, J_{SC}, *MPP* and *FF* (shaded gray) are shown.

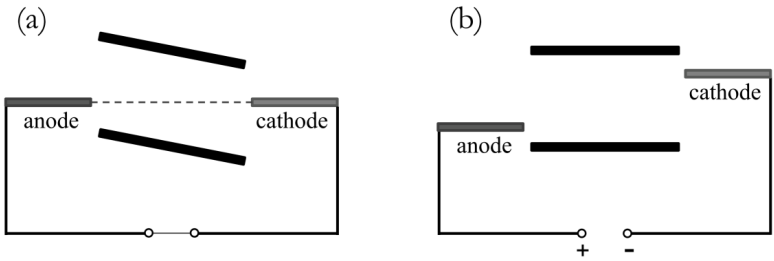

Figure 4.11 Device operation of an organic semiconductor layer sandwiched between metallic electrodes under (a) short-circuit condition (J_{sc}); (b) flat-band condition (V_{OC}). Band bending effects are neglected.[180]

With no voltage applied, the device is under short-circuit conditions and the measured photogenerated current density is the short-circuit current density, J_{SC}. This point corresponds to figure 4.11a. J_{SC} is related in a high extent to the bandgap of the absorbing polymer. A narrower bandgap ensures a better overlap with the solar spectrum and leads to higher current densities. Carrier

mobility, intermolecular interaction and molecular chain packing are also important parameters that influence J_{SC}.[180]

The voltage at which the photocurrent density is zero is the open-circuit voltage, V_{OC}. At this point the system is not necessarily in the flat band regime (figure 4.11b). Instead, flat band condition occurs when the curves in the dark and under illumination intersect. This occurs at the flat band (or compensation) voltage which ideally should correspond to the difference in work function of the electrodes.[181]

When the contacts between the active layer of the solar devices and the electrodes are ohmic, the value of V_{OC} is given by the difference between the HOMO of the donor material and the LUMO of the acceptor material. In the case of non-ohmic contacts, the maximum achievable V_{OC} is limited to the difference between the work functions of the electrodes. For polymer:fullerene bulk heterojunction photovoltaics, the following empirical equation was developed:[182]

$$V_{OC} = \left(\left| E^{Donor} HOMO \right| - \left| E^{PCBM} LUMO \right| - 0.3eV \right) / e \qquad (4.5)$$

Engineering a lower bandgap in order to achieve higher current densities as was suggested above can, unfortunately, have detrimental effects on the V_{OC} of the final devices and cancel out the favourable effect on the J_{SC}.[182] These parameters must therefore be considered simultanously when designing new materials. Figure 4.12 illustrates this issue.

MPP corresponds to the point at which the product of the current density and the voltage is maximized, $J_{MPP}.V_{MPP}$, and gives the maximum power output of the device (shaded gray in figure 4.10). When *MPP* is divided by the product

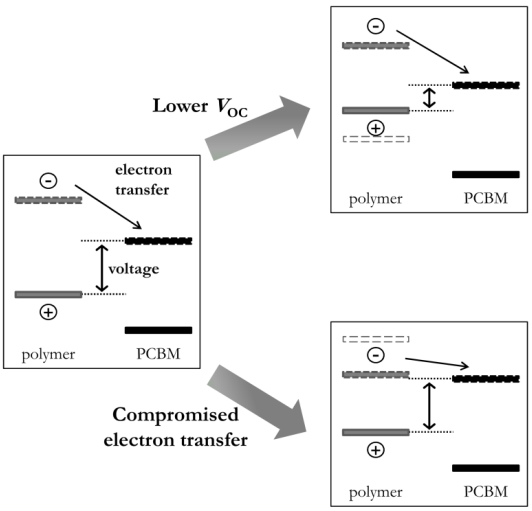

Figure 4.12 Effect of lowering the bandgap on the V_{OC} and electron transfer in a polymer:PCBM solar cell.

$J_{SC}.V_{OC}$, it gives the fill factor, *FF*. This parameter is a measure of the quality of the shape of the *J-V* curve.‡‡‡ The *FF* is affected by many parameters, such as charge mobility and balance, interface recombination and film morphology.[183] The ability to modulate the *FF* is crucial for solar cell performance improvement, but understanding it still remains a challenge.

4.6.2 Power conversion efficiency

The most important measure of photovoltaic performance is the power conversion efficiency (PCE or η). This is given by the maximum power that can be extracted from the device (P_{MPP}) per power of the incident light (P_{MPP}):[181]

$$\eta = \frac{P_{MPP}}{P_{light}} \tag{4.6}$$

‡‡‡ It is a measure of the *squareness* of the curve – the more square it is, the higher the FF.

Taking into account the photovoltaic parameters described in the previous section, the efficiency can be rewritten as

$$\eta = \frac{FF \cdot J_{SC} \cdot V_{OC}}{P_{light}} \tag{4.7}$$

η is the maximum value for the theoretical yield when the *FF*, J_{SC} and V_{OC} are maximized. These quantities are dependent on the intensity and the wavelength of the incoming light, therefore the power conversion efficiency is measured at standard light conditions.[20,181] The most common standard for photovoltaic characterization is briefly described in section 4.6.4.

4.6.3 External quantum efficiency

The external quantum efficiency (EQE), also known as the incident photon-to-current efficiency (IPCE), is used for determination of the spectral response of the solar cell and is an useful tool in the analysis of loss mechanisms. To determine the EQE, the ratio between the generated photocurrent and the incident photon flux is calculated as a function of wavelength. It can be derived from the spectral response, SR, which is the current in the external circuit (J_{SC}) per power of the incident light (P_{in}) given by

$$SR(\lambda) = \frac{J_{SC}(\lambda)}{P_{in}} \tag{4.8}$$

If the elementary charge (e) and the photon energy $\left(\frac{hc}{\lambda}\right)$ are considered:

$$EQE(\lambda) = \frac{hc}{\lambda e} \cdot SR(\lambda) = \frac{number \cdot of \cdot collected \cdot electrons}{number \cdot of \cdot incident \cdot photons} \tag{4.9}$$

This gives a measure of the overall efficiency of four processes: absorption (*A*), exciton diffusion (*ED*), charge separation (*CS*) and charge collection (*CC*):[181,184]

$$EQE_{\lambda} = \eta_{A} \cdot \eta_{ED} \cdot \eta_{CS} \cdot \eta_{CC} \tag{4.10}$$

Figure 4.13 shows an example of an EQE vs wavelength graph for a series of APFO-3:PCBM devices prepared from different solvents.[185]

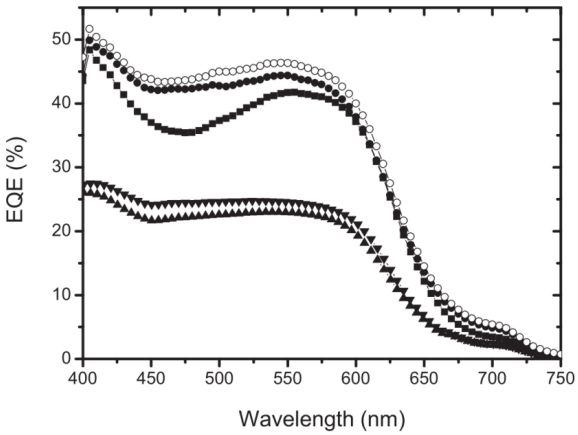

Figure 4.13 EQEs for APFO-3:PCBM photovoltaic devices made from different solvents.[185]

4.6.4 Solar radiation simulation

Reproducible, accurate and comparable solar cell performances call for standardized conditions of characterization.[186,187] Standard reporting conditions (SRC) have been specified, which include well-defined light intensity, incident spectral content and sample temperature. For rating the performance of terrestrial solar photovoltaics, the parameters are the ones shown in table 4.1.

Table 4.1 Standard reporting conditions for solar cell efficiency.

Standard reporting conditions	
Sun spectrum	AM1.5G
Light intensity	1000 W/m^2
Sample temperature	25ºC

AM1.5G (*air mass 1.5 global*), shown in figure 4.14, refers to the simulated solar spectrum corrected for scattering and absorption in the atmosphere, and measured at a 48º angle to the zenith, as defined by international standard norms (IEC 904-3 and ASTMG173-03).

The visible and near-infrared regions of the solar spectrum, ranging from 400 to 1400 nm, are the most relevant for solar cells, and a good overlap with the absorption range of the active materials is crucial for good photon harvesting and subsequent photovoltaic performance. Most polymer semiconductors absorb within the 350 – 650 nm range, falling short of the photon flux peak at around 700 nm (see figure 4.14). As a result, the development of low bandgap

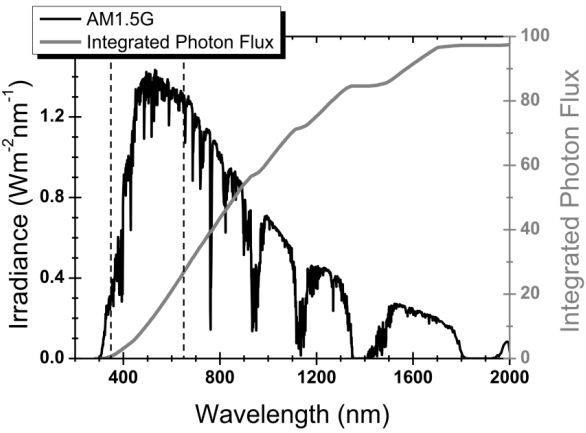

Figure 4.14 Standard solar spectrum AM1.5G (black line) and integrated photon flux (gray line), given as a percentage of the total number of photons. Vertical dashed lines mark the range of absorption of most conjugated polymers. [data source: http://rredc.nrel.gov/solar/spectra/am1.5/]

materials with wider and/or red-shifted light absorption ranges has been a major interest in the research community and new polymers with absorptions extending up to 900 nm[188,189] and more[190] have been reported.

4.6.5 Instrumentation

The solar devices were prepared and characterized at the group for Organic Semiconductors of Prof. Wolfgang Brütting (University of Augsburg, Germany). Characterization was done by measuring the current response of the devices in vacuum as a function of varying voltage. *J-V* curves were taken in the dark and under white light illumination from a solar simulator (LOT-ORIEL, Germany) equipped with a Xenon arc lamp and AM1.5G filters. Values were recorded using a Keithley 236 source measure unit. The different light intensities were set by using neutral density filters calibrated against a 1×1 cm^2 silicon reference cell (ReRa Solutions BV, The Netherlands).

Chapter 5

Summary of the papers

5.1 Paper I

Molecular orientation and composition at the surface of spin-coated polyfluorene:fullerene blend films A.S. Anselmo, A. Dzwilewski, K. Svensson, E. Moons *Journal of Polymer Science Part B: Polymer Physics*, **2013**, 51 (3), pp 176-182 (DOI: 10.1002/polb.23198)

In this paper, the outermost surface composition of blend films of APFO-3 and PCBM was analysed quantitatively and qualitatively with NEXAFS spectroscopy. Blend thin films in 50:50 and 20:80 weight ratios (APFO-3:PCBM) were spin-coated from chloroform (CF) and from chlorobenzene (CB). The analysis was done at two different depth regimes, by the use of PEY and TEY detection modes. Surface composition was obtained by fitting the blend spectra with a linear combination of the spectra of the pure components. The results showed the existence of vertical compositional gradients in the surface region of APFO-3:PCBM blend films, for both blend ratios and both solvents, with clear polymer-enrichment of the surface. Angle-resolved NEXAFS spectroscopy was used to study the molecular orientation in pure APFO-3 films and revealed a predominantly plane-on orientation of the polymer's conjugated system, stronger in the subsurface region than at the surface. We suggested that polymer chain packing at the surface may be disturbed by chain distortions arising from mechanisms of surface energy minimization. In the case of blend films, the orientational preference was less

pronounced and no difference between surface and subsurface was found. This weaker dichroism indicates a high miscibility between PCBM and APFO-3 that disturbs polymer chain organization. Given the similarities between the surface composition and organization of the blend thin films spin-coated from CF and CB, differences in solar cell efficiency reported elsewhere are expected to originate from bulk, and not surface, properties.

5.2 Paper II

Tuning the vertical phase separation in polyfluorene:fullerene blend films by polymer functionalization A.S. Anselmo, L. Lindgren, J. Rysz, A. Bernasik, A. Budkowski, M.R. Andersson, K. Svensson, J. van Stam, E. Moons *Chem. Mater.*, **2011**, 23 (9), pp 2295-2302 (DOI: 10.1021/cm1021596).

In this work, the nanomorphology and composition of blend films of three new polyfluorene copolymers, APFO-Green11, APFO-Green12 and APFO-Green13, with the fullerene derivative PCBM was investigated. These polymers were tailored for enhanced miscibility with PCBM by systematic changes in their side chains. To achieve this, small amounts of a monomer with modified side chains that can form hydrogen bonds with the side chain of PCBM were introduced during polymerization. The blend films were prepared in a 1:4 weight ratio (polymer:PCBM) and spin-coated from CF. In-depth organization was analysed with dSIMS. Depth profiles showed compositional variations that propagated throughout the film due to vertical phase separation. More pronounced vertical compositional variations were found for the blend with the more modified polymer. The films' surface morphology and composition were studied by TM-AFM and NEXAFS. Quantitative analysis of the surface composition was done through a linear combination fit of the NEXAFS spectra of the blends by using the spectra of the pure components. The resulting blend ratios revealed polymer-enrichment of the film surface for all three blends. This surface polymer-enrichment was stronger for the more

modified polymer, in agreement with dSIMS results. By using two different electron detection modes, PEY- and TEY-NEXAFS, it was possible to evaluate quantitatively the surface composition of the films in two different depth regimes. A vertical composition gradient was found to build up already in the first few nanometers of the surface of the blend films, a depth region which dSIMS could not resolve. Phase separation and polymer-enrichment of the free surface were stronger as the fraction of modified monomer, and hence the polymer's chemical miscibility with the fullerene, increased. The effect of these morphological changes on solar cell performance was studied in paper III.

5.3 Paper III

Polyfluorene copolymers with functionalized side chains: opto-electronic properties and solar cell performance A.S. Anselmo, L. Lindgren, K. Svensson, U. Hörmann, W. Brütting, J. van Stam, M.R. Andersson, A. Opitz, E. Moons
Manuscript

Here we continued to study the set of three polyfluorene copolymers with modified side chains that was the focus of paper II. We characterized their optical and electronic properties and studied their performance in photovoltaic devices when blended with the fullerene derivative PCBM (in 1:4 weight ratio, spin-coated from CF). The UV-Vis. absorption spectra of all three polymers are similar and yield an optical bandgap of 1.6 eV. The position of the HOMO and LUMO energy levels was determined both electrochemically, from square wave voltammograms, and spectroscopically, from valence band spectra. The values obtained from both methods showed no significant difference between the polymers. All cases showed the necessary energy level offset between polymer and PCBM for effective charge transfer. Photovoltaic parameters were extracted from the current-voltage dependence of polymer:PCBM devices made with the three polymers. The open-circuit voltage was 0.6 eV and the fill factors were high (ca 60%) for all devices. The photocurrent was the only

parameter influenced by the functionalization of the side chains, with lower values found for the devices made with the more modified polymer, i.e. the blend with the strongest vertical composition gradients. These lower photocurrent values, in turn, led to reduced efficiencies for these devices. The short-circuit current was shown to scale linearly with light intensity in all solar cells, ruling out serious asymmetry in charge mobilities, despite the vertical composition gradients. By optimizing layer thickness and blend ratio, the performance of devices based on these polymers may be improved.

5.4 Paper IV

Near-edge X-ray Absorption Fine Structure study of the C_{60}-derivative PCBM
I. Brumboiu, A.S. Anselmo, B. Brena, A. Dzwilewski, K. Svensson, E. Moons
Submitted to *Chemical Physics Letters*.

In this letter, we presented a combined experimental and theoretical study of the C1s NEXAFS spectrum of PCBM. The calculated spectrum, obtained from the single atomic contributions of the carbons that constitute the PCBM molecule, reproduces the experimentally obtained spectrum well. By comparing the experimental peaks with the contributions from specific segments of the molecule, we were able to assign the main resonances to specific molecular moieties. We analysed the π^*-resonance region in detail, particularly the first peak and its high energy shoulder. We found that this first peak is a result of 1s-LUMO transitions by core electrons from fullerene and phenyl carbon atoms. The shoulder localized ca 0.5 eV above the main π^*-peak was shown to arise partly from contributions from 1s to LUMO transitions of one particular carbon in the phenyl moiety and from transitions from 1s to higher orbitals of all the carbons in the fullerene cage, with the exception of the ones involved in the side chain attachment. However, the shoulder in the experimental data is more pronounced than what can be accounted for theoretically. Comparison of the experimental spectra obtained in PEY and TEY detection modes shows a

considerably larger shoulder in the more surface sensitive PEY spectrum, indicating a significant contribution from modified molecules at the surface, and a possible contribution from surface contaminants.

5.5 Paper V

Light-induced modification of the electronic structure of PCBM and C_{60} films
A.S. Anselmo, A. Dzwilewski, K. Svensson, E. Moons
Manuscript

In this work, we studied the effect of light exposure in ambient conditions on the electronic structure of PCBM in spin-coated films and of C_{60} in evaporated films. The films were exposed for different periods of time to light from an AM1.5 solar simulator and from a fluorescent bulb commonly used in the laboratory. The occupied and unoccupied molecular states of the molecules were analyzed by NEXAFS and XPS, respectively. We found damaged surfaces in both materials after exposure to AM1.5 light. The damages were more pronounced the longer the exposure time, leading to the destruction of the fullerene cage in less than 24 hours irradiation. Exposure to light from a fluorescent bulb led to a similar degradation behaviour, albeit less severe. Worth noting is the fact that a significant impact in the NEXAFS spectrum of PCBM was noticeable even for short exposure times, of the order of a few minutes, the time typically necessary for film preparation. Our results illustrate the need to control processing conditions, in particular air and light exposure, during OPV fabrication and characterization.

Chapter 6

Conclusions

In this work, we studied the morphology of spin-coated polymer:PCBM films and its influence on the performance of polymer photovoltaic devices, as well as the effect of light exposure in air on the electronic structure of fullerene films.

We found polymer-enrichment and compositional gradients at the surface of blend films of APFO-3:PCBM, independent of the spin-coating solvent. Previously, thin-films of this blend have shown a solvent-dependent bulk morphology, which was found to affect device performance. Our present results indicated that these differences in photovoltaic performance likely originated from variations in bulk properties, and not from surface effects.

It was also shown in this work that small modifications in the side chains of polyfluorene copolymers that affect polymer:fullerene interaction could induce stronger vertical phase separation, while not significantly impacting on the polymers' opto-electronic properties. Furthermore, it was shown that the performance of solar cells made with these polymers was influenced by the degree of side chain modification. The devices made with the polymer with the unmodified side chains showed a slightly higher photocurrent.

Finally, we found evidence of severe changes occurring at the surface of fullerene thin films when they were illuminated with white light in air. Both the

occupied and the unoccupied molecular orbitals of the materials were severely altered after exposure to light. Damages were evident even after a short exposure time, of the order of what is typically necessary for film preparation. By comparison with calculated NEXAFS spectra for the unmodified PCBM, we suggested a modification of the hybridization of the carbon atoms from sp^2-type to sp^3 upon illumination in air, indicative of the destruction of the fullerene cage.

References

(1) Hermann, W. A. *Energy* **2006**, *31*, 1685–1702.

(2) U.S. Energy Information Administration EIA - 2011 International Energy Outlook (http://www.eia.gov/oiaf/ieo/) **2011**, available online 07/12/2012.

(3) U.S. Department of Energy - What is the energy payback for PV? (http://www.nrel.gov/docs/fy05osti/37322.pdf) **2004**, available online 07/12/2012.

(4) Green, M. A.; Emery, K.; Hishikawa, Y.; Warta, W.; Dunlop, E. D. *Progress in Photovoltaics: Research and Applications* **2012**, *20*, 606–614.

(5) Li, G.; Zhu, R.; Yang, Y. *Nature Photonics* **2012**, *6*, 153–161.

(6) Kallman, H.; Pope, M. *Journal of Chemical Physics* **1959**, *30*, 585–586.

(7) Shirakawa, H.; Louis, E. J.; MacDiarmid, A. G.; Chiang, C. K.; Heeger, A. J. *Journal of the Chemical Society, Chemical Communications* **1977**, 578–580.

(8) The Nobel Prize in Chemistry 2000 (http://nobelprize.org/nobel_prizes/chemistry/laureates/2000/). *The Nobel Foundation* available online 10/12/2011.

(9) Deibel, C.; Dyakonov, V. *Reports on Progress in Physics* **2010**, *73*, 096401.

(10) Tang, C. W. *Applied Physics Letters* **1986**, *48*, 183–185.

(11) Sariciftci, N. S.; Smilowitz, L.; Heeger, A. J.; Wudl, F. *Science* **1992**, *258*, 1474–1476.

(12) Morita, S.; Zakhidov, A. A.; Yoshino, K. *Solid State Communications* **1992**, *82*, 249–252.

(13) Hiramoto, M.; Fujiwara, H.; Yokoyama, M. *Journal of Applied Physics* **1992**, *72*, 3781–3787.

(14) Yu, G.; Gao, J.; Hummelen, J. C.; Wudl, F.; Heeger, A. J. *Science* **1995**, *270*, 1789–1791.

(15) Halls, J. J. M.; Walsh, C. A.; Greenham, N. C.; Marseglia, E. A.; Friend, R. H.; Moratti, S. C.; Holmes, A. B. *Nature* **1995**, *376*, 498–500.

(16) Mullekom, H. van *Materials Science and Engineering: R: Reports* **2001**, *32*, 1–40.

(17) Halls, J. J. M.; Friend, R. H. In *Clean Electricity from Photovoltaics - Series on Photoconversion of Solar Energy Vol. 1*; Archer, M. D.; Hill, R., Eds.; Imperial College Press, 2001; pp. 377–433.

(18) Solomons, T. W. G. *Organic Chemistry*; 6th ed.; John Wiley & Sons, 1996.

(19) Kertesz, M.; Choi, C. H.; Yang, S. *Chemical Reviews* **2005**, *105*, 3448–3481.

(20) Brabec, C. J.; Dyakonov, V. In *Organic Photovoltaics - Concepts and Realization*; Brabec, C. J.; Dyakonov, V.; Parisi, J.; Sariciftci, N. S., Eds.; Springer-Verlag, 2003; pp. 1–56.

(21) Loos, J.; Bavel, S. van; Yang, X. In *Organic Photovoltaics - Materials, Device Physics, and Manufacturing Technologies*; Brabec, C.; Dyakonov, V.; Scherf, U., Eds.; Wiley-VCH, 2008; pp. 299–326.

(22) Hertel, D.; Bässler, H. *ChemPhysChem* **2008**, *9*, 666–688.

(23) Beaupré, S.; Boudreault, P.-L. T.; Leclerc, M. *Advanced Materials* **2010**, *22*, E6–E27.

(24) Zuo, Z.; Li, Y. *Polymer Bulletin* **2011**, *68*, 1425–1467.

(25) Mayukh, M.; Jung, I. H.; He, F.; Yu, L. *Journal of Polymer Science Part B: Polymer Physics* **2012**, *50*, 1057–1070.

(26) Son, H. J.; Carsten, B.; Jung, I. H.; Yu, L. *Energy & Environmental Science* **2012**, *5*, 8158–8170.

(27) Dresselhaus, S.; Dresselhaus, G.; Eklund, P. *Science of Fullerenes and Carbon Nanotubes*; Academic Press, 1996.

(28) Haddon, R. C.; Brus, L. E.; Raghavachari, K. *Chemical Physics Letters* **1986**, *13*, 165–169.

(29) Kroto, H. W.; Health, J. R.; O'Brien, S. C.; Curl, R. F.; Smalley, R. E. *Nature* **1985**, *318*, 162–163.

(30) The Nobel Prize in Chemistry 1996 (http://www.nobelprize.org/nobel_prizes/chemistry/laureates/1996/). *The Nobel Foundation* available online 10/12/2012.

(31) Krätschmer, W.; Lamb, L. D.; Fostiropoulos, K.; Huffman, D. R. *Nature* **1990**, *347*, 354–358.

(32) Gudaev, O. A.; Malinovsky, V. K.; Okotrub, A. V; Shevtsov, Y. V *Fullerene Science and Technology* **1998**, *6*, 433–443.

(33) Jarrett, P.; Pichler, K.; Newbould, R.; Friend, R. H. *Synthetic* **1996**, *77*, 35–38.

(34) Kronholm, D. F.; Hummelen, J. C. In *Organic Photovoltaics - Materials, Device Physics, and Manufacturing Technologies*; Brabec, C. J.; Dyakonov, V.; Scherf, U., Eds.; Wiley-VCH, 2010; pp. 155–178.

(35) Li, C.-Z.; Yip, H.-L.; Jen, A. K.-Y. *Journal of Materials Chemistry* **2012**, *22*, 4161–4177.

(36) Kraabel, B.; McBranch, D.; Sariciftci, N. S.; Moses, D.; Heeger, A. J. *Physical Review B* **1994**, *50*, 18543–18552.

(37) D'Souza, F.; Kadish, K. M. *Handbook of carbon nano materials*; World Scientific Publishing Co. Ltd., 2011.

(38) Bezmel'nitsyn, V. N.; Eletskii, A. V; Okun', M. V *Physics-Uspekhi* **1998**, *41*, 1091–1114.

(39) Hummelen, J. C.; Knight, B. W.; LePeq, F.; Wudl, F. *Journal of Organic Chemistry* **1995**, *60*, 532–538.

(40) Ferguson, A. J.; Blackburn, J. L.; Kopidakis, N. *Materials Letters* **2013**, *90*, 115–125.

(41) Wienk, M. M.; Kroon, J. M.; Verhees, W. J. H.; Knol, J.; Hummelen, J. C.; Hal, P. A. van; Janssen, R. A. J. *Angewandte Chemie (International ed. in English)* **2003**, *42*, 3371–3375.

(42) Guilén, C.; Herrero, J. In *Organic Photovoltaics - Materials, Device Physics, and Manufacturing Technologies*; Brabec, C.; Dyakonov, V.; Scherf, U., Eds.; Wiley-VCH, 2008; pp. 401–423.

(43) *Applied Photovoltaics*; Wenham, S. R.; Green, M. A.; Watt, M. E., Eds.; Earthscan, 2006.

(44) Sun, S.-S.; Bonner, C. E. In *Organic Photovoltaics - Mechanisms, Materials, and Devices*; Sun, S.-S.; Sariciftci, N. S., Eds.; CRC Press, 2005; pp. 183–213.

(45) Brabec, C. J. In *Organic Photovoltaics - Concepts and Realization*; Brabec, C. J.; Dyakonov, V.; Parisi, J.; Sariciftci, N. S., Eds.; Springer-Verlag, 2003; pp. 159–248.

(46) Jones, D. In *Organic Photovoltaics - Materials, Device Physics, and Manufacturing Technologies*; Brabec, C.; Dyakonov, V.; Scherf, U., Eds.; Wiley-VCH, 2008; pp. 57–91.

(47) Müller, C.; Wang, E.; Andersson, L. M.; Tvingstedt, K.; Zhou, Y.; Andersson, M. R.; Inganäs, O. *Advanced Functional Materials* **2010**, *20*, 2124–2131.

(48) Nilsson, S.; Bernasik, A.; Budkowski, A.; Moons, E. *Macromolecules* **2007**, *40*, 8291–8301.

(49) Li, G.; Shrotriya, V.; Huang, J.; Yao, Y.; Moriarty, T.; Emery, K.; Yang, Y. *Nature Materials* **2005**, *4*, 864–868.

(50) Yang, X.; Duren, J. K. J. van; Rispens, M. T.; Hummelen, J. C.; Janssen, R. A. J.; Michels, M. A. J.; Loos, J. *Advanced Materials* **2004**, *16*, 802–806.

(51) Björström, C. M.; Nilsson, S.; Bernasik, A.; Rysz, J.; Budkowski, A.; Zhang, F.; Inganäs, O.; Andersson, M. R.; Magnusson, K. O.; Moons, E. *Proceedings of SPIE* **2006**, *6192*, 61921X.

(52) Kim, Y. S.; Lee, Y.; Kim, J. K.; Seo, E.-O.; Lee, E.-W.; Lee, W.; Han, S.-H.; Lee, S.-H. *Current Applied Physics* **2010**, *10*, 985–989.

(53) Ho, P. K.-H.; Chua, L.-L.; Dipankar, M.; Gao, X. Y.; Qi, D. C.; Wee, A. T.-S.; Chang, J.-F.; Friend, R. H. *Advanced Materials* **2007**, *19*, 215–221.

(54) Walheim, S.; Böltau, M.; Mlynek, J.; Krausch, G.; Steiner, U. *Macromolecules* **1997**, *30*, 4995–5003.

(55) Gedde, U. W. *Polymer Physics*; Kluwer Academic Publishers, 2001.

(56) Flory, P. J. *Journal of Chemical Physics* **1941**, *9*, 660–660.

(57) Huggins, M. L. *Journal of Chemical Physics* **1941**, *9*, 440–440.

(58) Jones, R. A. L. *Soft Condensed Matter*; Oxford University Press, 2002.

(59) Arias, A. C. *Polymer Reviews* **2006**, *46*, 103–125.

(60) Bates, F. S. *Science* **1991**, *251*, 898–905.

(61) Lin, C. C.; Jonnalagadda, S. V; Balsara, N. P.; Han, C. C.; Krishnamoorti, R. *Macromolecules* **1996**, *29*, 661–669.

(62) Jones, R. A. L.; Kramer, E. J.; Rafailovich, M. H.; Sokolov, J.; Schwarz, S. A. *Physical Review* **1989**, *62*, 280–283.

(63) Jones, R. A. L.; Norton, L. J.; Kramer, E. J.; Bates, F. S.; Wiltzius, P. *Physical Review Letters* **1991**, *66*, 1326–1329.

(64) Genzer, J.; Kramer, E. *Physical Review Letters* **1997**, *78*, 4946–4949.

(65) Ton-That, C.; Shard, A. G.; Daley, R.; Bradley, R. H. *Macromolecules* **2000**, *33*, 8453–8459.

(66) Budkowski, A.; Bernasik, A.; Cyganik, P.; Raczkowska, J.; Penc, B.; Bergues, B.; Kowalski, K.; Rysz, J.; Janik, J. *Macromolecules* **2003**, *36*, 4060–4067.

(67) Sprenger, M.; Walheim, S.; Budkowski, A.; Steiner, U. *Materials Science* **2003**, *11*, 225–235.

(68) Raczkowska, J.; Bernasik, A.; Budkowski, A.; Sajewicz, K.; Penc, B.; Lekki, J.; Lekka, M.; Rysz, J.; Kowalski, K.; Czuba, P. *Macromolecules* **2004**, *37*, 7308–7315.

(69) Bernasik, A.; Wlodarczyk-Miskiewicz, J.; Luzny, W.; Kowalski, K.; Raczkowska, J.; Rysz, J.; Budkowski, A. *Synthetic Metals* **2004**, *144*, 253–257.

(70) Heriot, S. Y.; Jones, R. A. L. *Nature Materials* **2005**, *4*, 782–786.

(71) Jørgensen, M.; Norrman, K.; Krebs, F. C. *Solar Energy Materials and Solar Cells* **2008**, *92*, 686–714.

(72) Grossiord, N.; Kroon, J. M.; Andriessen, R.; Blom, P. W. M. *Organic Electronics* **2012**, *13*, 432–456.

(73) Lee, J. U.; Jung, J. W.; Jo, J. W.; Jo, W. H. *Journal of Materials Chemistry* **2012**, *22*, 24265.

(74) Jørgensen, M.; Norrman, K.; Gevorgyan, S. A.; Tromholt, T.; Andreasen, B.; Krebs, F. C. *Advanced Materials* **2012**, *24*, 580–612.

(75) *Stability and Degradation of Organic and Polymer Solar Cells*; Krebs, F. C., Ed.; John Wiley & Sons, 2012.

(76) Reese, M. O.; Gevorgyan, S. A.; Jørgensen, M.; Bundgaard, E.; Kurtz, S. R.; Ginley, D. S.; Olson, D. C.; Lloyd, M. T.; Morvillo, P.; Katz, E. A.; Elschner, A.; Haillant, O.; Currier, T. R.; Shrotriya, V.; Hermenau, M.; Riede, M.; R. Kirov, K.; Trimmel, G.; Rath, T.; Inganäs, O.; Zhang, F.; Andersson, M.; Tvingstedt, K.; Lira-Cantu, M.; Laird, D.; McGuiness, C.; Gowrisanker, S. (Jimmy); Pannone, M.; Xiao, M.; Hauch, J.; Steim, R.; DeLongchamp, D. M.; Rösch, R.; Hoppe, H.; Espinosa, N.; Urbina, A.; Yaman-Uzunoglu, G.; Bonekamp, J.-B.; Breemen, A. J. J. M. van; Girotto, C.; Voroshazi, E.; Krebs, F. C. *Solar Energy Materials and Solar Cells* **2011**, *95*, 1253–1267.

(77) Manceau, M.; Bundgaard, E.; Carlé, J. E.; Hagemann, O.; Helgesen, M.; Søndergaard, R.; Jørgensen, M.; Krebs, F. C. *Journal of Materials Chemistry* **2011**, *21*, 4132–4141.

(78) Manceau, M.; Helgesen, M.; Krebs, F. C. *Polymer Degradation and Stability* **2010**, *95*, 2666–2669.

(79) Chambon, S.; Rivaton, A.; Gardette, J.-L.; Firon, M. *Solar Energy Materials and Solar Cells* **2007**, *91*, 394–398.

(80) Reese, M. O.; Nardes, A. M.; Rupert, B. L.; Larsen, R. E.; Olson, D. C.; Lloyd, M. T.; Shaheen, S. E.; Ginley, D. S.; Rumbles, G.; Kopidakis, N. *Advanced Functional Materials* **2010**, *20*, 3476–3483.

(81) Johnson, B. H.; Allagoa, E.; Thomas, R. L.; Stettler, G.; Wallis, M.; Peel, J. H.; Adalsteinsson, T.; McNelis, B. J.; Barber, R. P. *Solar Energy Materials and Solar Cells* **2010**, *94*, 537–541.

(82) Matsuo, Y.; Ozu, A.; Obata, N.; Fukuda, N.; Tanaka, H.; Nakamura, E. *Chemical Communications* **2012**, *48*, 3878–3880.

(83) Gevorgyan, S. A.; Krebs, F. C. *Chemistry of Materials* **2008**, *20*, 4386–4390.

(84) Sivula, K.; Luscombe, C. K.; Thompson, B. C.; Fréchet, J. M. J. *Journal of the American Chemical Society* **2006**, *128*, 13988–13989.

(85) Zhang, Y.; Yip, H.-L.; Acton, O.; Hau, S. K.; Huang, F.; Jen, A. K.-Y. *Chemistry of Materials* **2009**, *21*, 2598–2600.

(86) Dress, M.; Hoppe, H.; Winder, C.; Neugebauer, H.; Sariciftci, N. S.; Schwinger, W.; Schäffler, F.; Topf, C.; Scharber, M. C.; Ziu, Z.; Gaudiana, R. *Journal of Materials Chemistry* **2005**, *15*, 5158–5163.

(87) Kim, B. J.; Miyamoto, Y.; Ma, B.; Fréchet, J. M. J. *Advanced Functional Materials* **2009**, *19*, 2273–2281.

(88) Farinhas, J.; Ferreira, Q.; Paolo, R. E. Di; Alcácer, L.; Morgado, J.; Charas, A. *Journal of Materials Chemistry* **2011**, *21*, 12511–12519.

(89) Griffini, G.; Douglas, J. D.; Piliego, C.; Holcombe, T. W.; Turri, S.; Fréchet, J. M. J.; Mynar, J. L. *Advanced Materials* **2011**, *23*, 1660–1664.

(90) Li, X.; Chen, L.; Chen, Y.; Li, F.; Yao, K. *Organic Electronics* **2012**, *13*, 104–113.

(91) Kim, H. J.; Han, A.-R.; Cho, C.-H.; Kang, H.; Cho, H.-H.; Lee, M. Y.; Fréchet, J. M. J.; Oh, J. H.; Kim, B. J. *Chemistry of Materials* **2012**, *24*, 215–221.

(92) Sivula, K.; Ball, Z. T.; Watanabe, N.; Fréchet, J. M. J. *Advanced Materials* **2006**, *18*, 206–210.

(93) Tsai, J.-H.; Lai, Y.-C.; Higashihara, T.; Lin, C.-J.; Ueda, M.; Chen, W.-C. *Macromolecules* **2010**, *43*, 6085–6091.

(94) Lee, J. U.; Jung, J. W.; Emrick, T.; Russell, T. P.; Jo, W. H. *Nanotechnology* **2010**, *21*, 105201.

(95) Kim, J. B.; Allen, K.; Oh, S. J.; Lee, S.; Toney, M. F.; Kim, Y. S.; Kagan, C. R.; Nuckolls, C.; Loo, Y.-L. *Chemistry of Materials* **2010**, *22*, 5762–5773.

(96) Jönsson, S. K. M.; Carlegrim, E.; Zhang, F.; Salaneck, W. R.; Fahlman, M. *Japanese Journal of Applied Physics* **2005**, *44*, 3695–3701.

(97) Krebs, F. C.; Norrman, K. *Progress in Photovoltaics: Research and Applications* **2007**, *15*, 697–712.

(98) Yu, Z.; Niu, X.; Liu, Z.; Pei, Q. *Advanced Materials* **2011**, *23*, 3989–3994.

(99) Lipomi, D. J.; Tee, B. C.-K.; Vosgueritchian, M.; Bao, Z. *Advanced Materials* **2011**, *23*, 1771–1775.

(100) Iwan, A.; Chuchmała, A. *Progress in Polymer Science* **2012**, 1–24.

(101) Nardes, A. M.; Kemerink, M.; Kok, M. M. de; Vinken, E.; Maturova, K.; Janssen, R. A. J. *Organic Electronics* **2008**, *9*, 727–734.

(102) Jong, M. P. de; IJzendoorn, L. J. van; Voigt, M. J. A. de *Applied Physics Letters* **2000**, *77*, 2255–2257.

(103) Bulle-Lieuwma, C.; Gennip, W. J. H. van; Duren, J. K. J. van; Jonkheijm, P.; Janssen, R. A. J.; Niemantsverdriet, J. W. *Applied Surface Science* **2003**, *203-204*, 547–550.

(104) Kawano, K.; Pacios, R.; Poplavskyy, D.; Nelson, J.; Bradley, D. D. C.; Durrant, J. R. *Solar Energy Materials and Solar Cells* **2006**, *90*, 3520–3530.

(105) Svensson, M.; Zhang, F.; Inganäs, O.; Andersson, M. R. *Synthetic Metals* **2003**, *135-136*, 137–138.

(106) Svensson, M.; Zhang, F.; Veenstra, S. C.; Verhees, W. J. H.; Hummelen, J. C.; Kroon, J. M.; Inganäs, O.; Andersson, M. R. *Advanced Materials* **2003**, *15*, 988–991.

(107) Inganäs, O.; Zhang, F.; Andersson, M. R. *Accounts of Chemical Research* **2009**, *42*, 1731–1739.

(108) Havinga, E. E.; Hoeve, W. ten; Wynberg, H. *Polymer Bulletin* **1992**, *29*, 119–126.

(109) Kitamura, C.; Tanaka, S.; Yamashita, Y. *Chemistry of Materials* **1996**, *8*, 570–578.

(110) Hellström, S.; Zhang, F.; Inganäs, O.; Andersson, M. R. *Dalton Transactions* **2009**, *45*, 10032–10039.

(111) Gedefaw, D.; Zhou, Y.; Hellström, S.; Lindgren, L.; Andersson, L. M.; Zhang, F.; Mammo, W.; Inganäs, O.; Andersson, M. R. *Journal of Materials Chemistry* **2009**, *19*, 5359–5363.

(112) Inganäs, O.; Svensson, M.; Zhang, F.; Gadisa, A.; Persson, N. K.; Wang, X.; Andersson, M. R. *Applied Physics A: Materials Science & Processing* **2004**, *79*, 31–35.

(113) Admassie, S.; Inganäs, O.; Mammo, W.; Perzon, E.; Andersson, M. R. *Synthetic Metals* **2006**, *156*, 614–623.

(114) Al-Ibrahim, M.; Roth, H.-K.; Schroedner, M.; Konkin, A.; Zhokhavets, U.; Gobsch, G.; Scharff, P.; Sensfuss, S. *Organic Electronics* **2005**, *6*, 65–77.

(115) Kiel, J. W.; Kirby, B. J.; Majkrzak, C. F.; Maranville, B. B.; Mackay, M. E. *Soft Matter* **2010**, *6*, 641–646.

(116) Søndergaard, R. R.; Hösel, M.; Krebs, F. C. *Journal of Polymer Science Part B: Polymer Physics* **2013**, *51*, 16–34.

(117) Lawrence, C. J. *Physics of Fluids* **1988**, *31*, 2786–2795.

(118) Bornside, D. E.; Macosko, C. W.; Scriven, L.-E. E. *Journal of Imaging Technology* **1987**, *13*, 122–130.

(119) Flack, W. W.; Soong, D. S.; Bell, A. T.; Hess, D. W. *Journal of Applied Physics* **1984**, *56*, 1199–1206.

(120) Meyerhofer, D. *Journal of Applied Physics* **1978**, *49*, 3993–3997.

(121) Chang, C.-C.; Pai, C.-L.; Chen, W.-C.; Jenekhe, S. A. *Thin Solid Films* **2005**, *479*, 254–260.

(122) Strawhecker, K. E.; Kumar, S. K.; Douglas, J. F.; Karim, A. *Macromolecules* **2001**, *34*, 4669–4672.

(123) Shaheen, S. E.; Brabec, C. J.; Sariciftci, N. S.; Padinger, F.; Fromherz, T.; Hummelen, J. C. *Applied Physics Letters* **2001**, *78*, 841–843.

(124) Rispens, M. T.; Meetsma, A.; Rittberger, R.; Brabec, C. J.; Sariciftci, N. S.; Hummelen, J. C. *Chemical Communications* **2003**, 2116–2118.

(125) Ma, W.; Yang, C.; Gong, X.; Lee, K.; Heeger, A. J. *Advanced Functional Materials* **2005**, *15*, 1617–1622.

(126) Kim, Y.; Cook, S.; Tuladhar, S. M.; Choulis, S. A.; Nelson, J.; Durrant, J. R.; Bradley, D. D. C.; Giles, M.; McCulloch, I.; Ha, C.-S.; Ree, M. *Nature Materials* **2006**, *5*, 197–203.

(127) Yang, X.; Loos, J. *Macromolecules* **2007**, *40*, 1353–1362.

(128) Brabec, C. J.; Gowrisanker, S.; Halls, J. J. M.; Laird, D.; Jia, S.; Williams, S. P. *Advanced Materials* **2010**, *22*, 3839–3856.

(129) Salleo, A.; Kline, R. J.; DeLongchamp, D. M.; Chabinyc, M. L. *Advanced Materials* **2010**, *22*, 3812–3838.

(130) Chen, L.-M.; Xu, Z.; Hong, Z.; Yang, Y. *Journal of Materials Chemistry* **2010**, *20*, 2575–2598.

(131) Slota, J. E.; He, X.; Huck, W. T. S. *Nano Today* **2010**, *5*, 231–242.

(132) Lee, S. S.; Loo, Y.-L. *Annual Review of Chemical and Biomolecular Engineering* **2010**, *1*, 59–78.

(133) Brabec, C. J.; Heeney, M.; McCulloch, I.; Nelson, J. *Chemical Society Reviews* **2011**, *40*, 1185–1199.

(134) Ruderer, M. A.; Müller-Buschbaum, P. *Soft Matter* **2011**, *7*, 5482–5493.

(135) Liu, F.; Gu, Y.; Jung, J. W.; Jo, W. H.; Russell, T. P. *Journal of Polymer Science Part B: Polymer Physics* **2012**, *50*, 1018–1044.

(136) Hoppe, H.; Niggemann, M.; Winder, C.; Kraut, J.; Hiesgen, R.; Hinsch, A.; Meissner, D.; Sariciftci, N. S. *Advanced Functional Materials* **2004**, *14*, 1005–1011.

(137) Watts, B.; McNeill, C. R. *Macromolecular Rapid Communications* **2010**, *31*, 1706–1712.

(138) Yang, X.; Duren, J. K. J. van; Janssen, R. A. J.; Michels, M. A. J.; Loos, J. *Macromolecules* **2004**, *37*, 2151–2158.

(139) Duren, J. K. D. van; Yang, X.; Loos, J.; Bulle-Lieuwma, C. W. T.; Sieval, A. B.; Hummelen, J. C.; Janssen, R. A. J. *Advanced Functional Materials* **2004**, *14*, 425–434.

(140) Herzing, A. A.; Richter, L. J.; Anderson, I. M. *Journal of Physical Chemistry C* **2010**, *114*, 17501–17508.

(141) Martens, T. *Synthetic Metals* **2003**, *138*, 243–247.

(142) Xu, Z.; Chen, L.-M.; Yang, G.; Huang, C.-H.; Hou, J.; Wu, Y.; Li, G.; Hsu, C.-S.; Yang, Y. *Advanced Functional Materials* **2009**, *19*, 1227–1234.

(143) Felicissimo, M. P.; Jarzab, D.; Gorgoi, M.; Forster, M.; Scherf, U.; Scharber, M. C.; Svensson, S.; Rudolf, P.; Loi, M. A. *Journal of Materials Chemistry* **2009**, *19*, 4899–4901.

(144) Campoy-Quiles, M.; Ferenczi, T.; Agostinelli, T.; Etchegoin, P. G.; Kim, Y.; Anthopoulos, T. D.; Stavrinou, P. N.; Bradley, D. D. C.; Nelson, J. *Nature Materials* **2008**, *7*, 158–164.

(145) Björström, C. M.; Bernasik, A.; Rysz, J.; Budkowski, A.; Nilsson, S.; Svensson, M.; Andersson, M. R.; Magnusson, K. O.; Moons, E. *Journal of Physics: Condensed Matter* **2005**, *17*, L529–L534.

(146) Björström Svanström, C. M.; Rysz, J.; Bernasik, A.; Andersson, M. R.; Budkowski, A.; Zhang, F.; Inganäs, O.; Magnusson, K. O.; Benson-Smith, J. J.; Nelson, J.; Moons, E. *Advanced Materials* **2009**, *21*, 4398–4403.

(147) Bernasik, A.; Rysz, J.; Budkowski, A.; Kowalski, K.; Camra, J.; Jedliński, J. *Macromolecular Rapid Communications* **2001**, *22*, 829–834.

(148) Bavel, S. van; Sourty, E.; With, G. de; Loos, J. *Nano Letters* **2009**, *9*, 507–513.

(149) Andersson, B. V.; Herland, A.; Masich, S.; Inganäs, O. *Nano Letters* **2009**, *9*, 853–855.

(150) Oosterhout, S. D.; Wienk, M. M.; Bavel, S. S. van; Thiedmann, R.; Koster, L. J. A.; Gilot, J.; Loos, J.; Schmidt, V.; Janssen, R. A. J. *Nature Materials* **2009**, *8*, 818–824.

(151) Bavel, S. van; Sourty, E.; With, G. de; Frolic, K.; Loos, J. *Macromolecules* **2009**, *42*, 7396–7403.

(152) Germack, D. S.; Chan, C. K.; Hamadani, B. H.; Richter, L. J.; Fischer, D. A.; Gundlach, D. J.; DeLongchamp, D. M. *Applied Physics Letters* **2009**, *94*, 233303.

(153) Germack, D. S.; Chan, C. K.; Kline, R. J.; Fischer, D. A.; Gundlach, D. J.; Toney, M. F.; Richter, L. J.; DeLongchamp, D. M. *Macromolecules* **2010**, *43*, 3828–3836.

(154) Xue, B.; Vaughan, B.; Poh, C.-H.; Burke, K. B.; Thomsen, L.; Stapleton, A.; Zhou, X.; Bryant, G. W.; Belcher, W.; Dastoor, P. C. *The Journal of Physical Chemistry C* **2010**, *114*, 15797–15805.

(155) Tillack, A. F.; Noone, K. M.; Macleod, B. A.; Nordlund, D.; Nagle, K. P.; Bradley, J. A.; Hau, S. K.; Yip, H.-L.; Jen, A. K.-Y.; Seidler, G. T.; Ginger, D. S. *ACS Applied Materials & Interfaces* **2011**, *3*, 726–32.

(156) Binnig, G.; Quate, C. F.; Gerber, C. *Physical Review Letters* **1986**, *56*, 930–933.

(157) Meyer, E.; Hug, H. J.; Bennewitz, R. *Scanning Probe Microscopy*; Springer-Verlag, 2004.

(158) *Handbook of Surfaces and Interfaces of Materials - Surface and Interface Analysis and Properties Vol.2*; Nalwa, H. S., Ed.; Academic Press, 2001.

(159) Briggs, D. *Surface analysis of polymers by XPS and static SIMS*; Cambridge University Press, 1998.

(160) Mahoney, C. M. *Mass Spectrometry Reviews* **2010**, *29*, 247–293.

(161) EAG Labs SIMS Theory Tutorial (http://www.eaglabs.com/training/tutorials/sims_theory_tutorial/) **2011**, available online 27/06/2011.

(162) Bernasik, A.; Rysz, J.; Budkowski, A.; Kowalski, K.; Camra, J.; Jedliński, J. In *ECASIA 97 (7th Conference on Applications of Surface and Interface Analysis)*; Olefjord, I.; Nyborg, L.; Briggs, D., Eds.; John Wiley & Sons, 1997; pp. 775–778.

(163) Stöhr, J. *NEXAFS Spectroscopy*; Springer-Verlag, 1996.

(164) Watts, B.; Thomsen, L.; Dastoor, P. *Journal of Electron Spectroscopy and Related Phenomena* **2006**, *151*, 105–120.

(165) Ade, H.; Urquhart, S. G. In *Chemical Applications of Synchrotron Radiation*; Sham, T. K., Ed.; World Scientific Publishing Co. Ltd., 2002.

(166) Ade, H.; Watts, B.; Swaraj, S.; McNeill, C.; Thomsen, L.; Belcher, W.; Dastoor, P. C. *Journal of Physics: Conference Series* **2009**, *186*, 012102.

(167) McNeill, C. R.; Watts, B.; Thomsen, L.; Belcher, W. J.; Kilcoyne, A. L. D.; Greenham, N. C.; Dastoor, P. C. *Small* **2006**, *2*, 1432–1435.

(168) Stöhr, J.; Outka, D. A. *Physical Review B* **1987**, *36*, 7891–7905.

(169) DeLongchamp, D. M.; Lin, E. K.; Fischer, D. A. *Proceedings of SPIE* **2005**, *5940*, 59400A.

(170) Genzer, J.; Sivaniah, E.; Kramer, E. J.; Wang, J.; Körner, H.; Xiang, M.; Yang, S.; Ober, C. K.; Char, K.; Chaudhury, M. K.; Dekoven, B. M.; Bubeck, R. A.; Fischer, D. A.; Sambasivan, S. *Materials Research Society Symposium Proceedings* **1998**, *524*, 365–370.

(171) Watts, B.; Ade, H. *Journal of Electron Spectroscopy and Related Phenomena* **2008**, *162*, 49–55.

(172) Hertz, H. *Annalen der Physik* **1887**, *267*, 983–1000.

(173) Einstein, A. *Annalen der Physik* **1905**, *322*, 132–148.

(174) Lüth, H. *Solid Surfaces, Interfaces and Thin Films*; 4th ed.; Springer-Verlag, 2001.

(175) Zharnikov, M.; Frey, S.; Heister, K.; Grunze, M. *Journal of Electron Spectroscopy and Related Phenomena* **2002**, *124*, 15–24.

(176) Seah, M. P.; Dench, W. A. *Surface and Interface Analysis* **1979**, *1*, 2–11.

(177) Siegbahn, K.; Nordling, C.; Fahlman, A.; Hamrin, K.; Hedman, J.; Ndberg, R.; Johansson, C.; Bergmark, T.; Karlsson, S.-E.; Lindgren, I.;

Lindgren, B. *Atomic, Molecular and Solid-State-Structure Studied by Means of Electron Spectroscopy*; Almquist & Wiksells, 1967; Vol. 20.

(178) Gao, Y. *Materials Science and Engineering: R: Reports* **2010**, *68*, 39–87.

(179) Harris, D. C. *Quantitative Chemical Analysis*; 7th ed.; W. H. Freeman and Company, 2007.

(180) Hoppe, H.; Sariciftci, N. S. In *Photoresponsive Polymers II*; Marder, S. R.; Lee, K.-S., Eds.; Springer Berlin Heidelberg, 2008; pp. 1–86.

(181) Moliton, A.; Nunzi, J. *Polymer International* **2006**, *55*, 583–600.

(182) Scharber, M. C.; Mühlbacher, D.; Koppe, M.; Denk, P.; Waldauf, C.; Heeger, A. J.; Brabec, C. J. *Advanced Materials* **2006**, *18*, 789–794.

(183) Blom, P. W. M.; Mihailetchi, V. D.; Koster, L. D. A.; Markov, D. E. *Advanced Materials* **2007**, *19*, 1551–1566.

(184) Wang, X.; Liu, D.; Li, J. *Frontiers of Chemistry in China* **2010**, *5*, 45–60.

(185) Zhang, F.; Jespersen, K. G.; Björström, C.; Svensson, M.; Andersson, M. R.; Sundström, V.; Magnusson, K.; Moons, E.; Yartsev, A.; Inganäs, O. *Advanced Functional Materials* **2006**, *16*, 667–674.

(186) Shrotriya, V.; Li, G.; Yao, Y.; Moriarty, T.; Emery, K.; Yang, Y. *Advanced Functional Materials* **2006**, *16*, 2016–2023.

(187) Smestad, G. P.; Krebs, F. C.; Lampert, C. M.; Granqvist, C. G.; Chopra, K. L.; Mathew, X.; Takakura, H. *Solar Energy Materials and Solar Cells* **2008**, *92*, 371–373.

(188) Mühlbacher, D.; Scharber, M.; Morana, M.; Zhu, Z.; Waller, D.; Gaudiana, R.; Brabec, C.; Mühlbacher, B. D. *Advanced Materials* **2006**, *18*, 2884–2889.

(189) Peet, J.; Kim, J. Y.; Coates, N. E.; Ma, W. L.; Moses, D.; Heeger, A. J.; Bazan, G. C. *Nature Materials* **2007**, *6*, 497–500.

(190) Wang, T.-L.; Yang, C.-H.; Shieh, Y.-T.; Chen, Y.-C.; Ho, T.-H.; Chen, C.-H. *Solar Energy Materials and Solar Cells* **2012**, *107*, 298–306.

(191) Shockley, W.; Queisser, H. J. *Journal of Applied Physics* **1961**, *32*, 510–519.

List of abbreviations and acronyms

[60]-PCBM	The same as PCBM;
[70]-PCBM	[6,6]-phenyl-C_{71} butyric acid methyl ester;
A	Absorption;
AEY	Auger electron yield;
AFM	Atomic force microscopy;
AM1.5G	Air mass 1.5 global;
APFO	Alternating polyfluorene copolymer;
APFO-3	poly[(9,9-dioctylfluorenyl-2,7-diyl)-co-5,5-(4',7'-di-2-thienyl-2',1',3'-benzothiadiazole];
BHJ	Bulk heterojunction;
C_{60}	[60]-fullerene, buckminsterfullerene;
C_{70}	[70]-fullerene;
CB	Chlorobenzene;
CC	Charge collection;
CF	Chloroform;
CS	Charge separation;
D/A	Donor/Acceptor;
d5-PCBM	Pentadeuterated PCBM;
D-A-D	Donor-acceptor-donor;
dSIMS	Dynamic secondary ion mass spectrometry;
EA	Electron affinity;
ED	Exciton diffusion;
E_g	Energy gap or bandgap;
EQE	External quantum efficiency;

ESCA	Electron spectroscopy for chemical analysis;
F8DTBT	The same as APFO-3;
FF	Fill factor;
HOMO	Highest Occupied Molecular Orbital;
HOPG	Highly oriented pyrolytic graphite;
IP	Ionization potential;
IPCE	Incident photon-to-current efficiency;
ISOS	International summit on OPV stability;
ITO	indium tin oxide;
J_{SC}	Short-circuit current density;
LBPF5	The same as APFO-3;
LUMO	Lowest Unoccupied Molecular Orbital;
MALDI-TOF	Matrix-assisted laser desorption/ionization-time-of-flight mass spectrometry;
MCP	Multi-channel plate;
MIM	Metal-insulator-metal;
M_n	Number-average molecular weight;
MPP	Maximum power point;
M_w	Weight-average molecular weight;
NEXAFS	Near-edge X-ray absorption fine structure;
OPV	Organic photovoltaics;
P3HT	poly(3-hexylthiophene);
PCBM	[6,6]-phenyl-C_{61} butyric acid methyl ester, the same as [60]-PCBM;
PCE	Power conversion efficiency;
PDI	Polydispersity index;
PEDOT:PSS	poly(3,4-ethylendioxythiophene):poly(styrenesulfonate);

PEY	Partial electron yield;
PFDTBT	The same as APFO-3;
PFO-DBT	The same as APFO-3;
PPV	Poly-phenylenevinylene;
PSS	Poly(styrenesulfonate);
PV	Photovoltaic;
RBS	Rutherford backscattering spectrometry;
SEC	Size exclusion chromatography;
SEM	Scanning electron microscopy;
SR	Spectral response;
STXM	Scanning Transmission X-ray microscopy;
T_c	Critical temperature;
TEM	Transmission electron microscopy;
TEY	Total electron yield;
TM-AFM	Tapping mode atomic force microscopy;
UPS	Ultraviolet photoelectron spectroscopy;
UV-Vis.	Ultraviolet-Visible;
VASE	Variable-angle spectroscopic ellipsometry;
V_{OC}	Open-circuit voltage;
XPS	X-ray photoelectron spectroscopy.